POLITECNICO DI TORINO
Repository ISTITUZIONALE

A computational efficient, multi-domain numerical framework for modelling fuel cell - battery powered powertrains

Original
A computational efficient, multi-domain numerical framework for modelling fuel cell - battery powered powertrains / Brusasco, Alessandro; Bonfanti, Mauro; Balestrieri, Francesco; Gennaro, Giulio; Melchiorre, Matteo; Mauro, Stefano. - In: ENERGY CONVERSION AND MANAGEMENT. X. - ISSN 2590-1745. - 29:(2026). [10.1016/j.ecmx.2026.101527]

Availability:
This version is available at: 11583/3006681 since: 2026-01-19T07:39:04Z

Publisher:
Elsevier

Published
DOI:10.1016/j.ecmx.2026.101527

Terms of use:

This article is made available under terms and conditions as specified in the corresponding bibliographic description in the repository

Publisher copyright

(Article begins on next page)

29 April 2026

Energy Conversion and Management: X 29 (2026) 101527

Contents lists available at ScienceDirect

Energy Conversion and Management: X

journal homepage: www.sciencedirect.com/journal/energy-conversion-and-management-x

A computational efficient, multi-domain numerical framework for modelling fuel cell–battery powered powertrains

Alessandro Brusasco [a,*], Mauro Bonfanti [a,*], Francesco Balestrieri [a], Giulio Gennaro [b], Matteo Melchiorre [a], Stefano Mauro [a]

[a] Department of Mechanical and Aerospace Engineering, Politecnico di Torino, Torino, 10129, Italy
[b] VULKAN Italia Srl, Novi Ligure, 15067, Italy

ARTICLE INFO

Keywords:
Electric powertrain
Electric transport
Analytical model
Fuel cell
Battery

ABSTRACT

The global drive to decarbonize the transportation sector has intensified the adoption of emission-free powertrains, increasing the demand for high-fidelity yet computationally efficient modelling tools to support propulsion design, control development, and virtual testing. In this context, this paper presents a physics-based, system-level model of a fully electric propulsion system integrating a Proton Exchange Membrane fuel cell (PEMFC) and a lithium-ion battery pack. The proposed framework adopts a multi-domain 0D formulation, in which the fuel cell system, battery, power electronics and electric motor are consistently coupled through mechanistic governing equations, capturing the dominant electrochemical, gas, thermal, electrical, mechanical, and control interactions. Numerical comparison against a commercially available MATLAB-Simscape benchmark under real-world maritime load cycles demonstrates an overall accuracy of 98.87 % across key variables, while reducing the average simulation time to about one-fortieth of the benchmark computation time. The proposed model provides a reliable platform to support Digital Twin development, control design, and powertrain optimization. To advance sustainable transportation research, the model has been made open source and is accessible via a dedicated GitHub repository.

1. Introduction

The global energy sector is undergoing a fundamental transformation, shifting from fossil fuels to zero-emission energy sources [1]. The transportation sector, among the largest contributors to greenhouse gas emissions and pollutants, has significant adverse impacts on both the environment and public health [2]. In this context, hydrogen-powered fuel cells (FC) are considered a promising alternative to fossil fuel [3], offering emission-free powertrains with high efficiency and short refuelling times [4], comparable to internal combustion engine vehicles [5]. Compared to purely battery-electric solutions, hydrogen FC systems provide higher volumetric energy densities, in the range $0.33\,\mathrm{kW\,h\,L^{-1}}$ to $0.51\,\mathrm{kW\,h\,L^{-1}}$ depending on storage technology [6], versus approximately $0.14\,\mathrm{kW\,h\,L^{-1}}$ for Li-ion batteries [6]. Among the available technologies, Proton Exchange Membrane fuel cells (PEMFC) are the most adopted in transport thanks to their high efficiency, low operating temperature and high power density [7]. However, their limited dynamic response reduces the capability to track rapid load variations, so they are usually coupled with batteries that manage fast transients. This hybridization introduces non-trivial dynamic interactions among subsystems, motivating accurate system-level modelling to capture the overall dynamics and optimize performance. PEMFC powertrain models are typically classified as mechanistic (physics-based), empirical, or data-driven [8]. This distinction becomes critical at full system level, where the fuel cell stack must be modelled together with the balance of plant (BoP), including hydrogen storage, air compression, humidification and thermal management. Such systems are inherently complex, as they involve tightly coupled electrochemical, gas, thermal and electrical phenomena. Data-driven models act as black boxes trained on large datasets [9], while empirical models use simplified correlations derived from experiments or detailed mechanistic models [9]. Although computationally efficient, these two classes are less suitable when a detailed physical and chemical interpretation of system behaviour is required, for which mechanistic models are preferred [8].

Mechanistic models represent mass, energy and charge transport through explicit conservation equations, typically formulated via mass, energy and species balances coupled with fluid dynamics, heat transfer and electrochemical kinetics. Reported PEMFC models span different fidelity levels, namely three-dimensional (3D), two-dimensional (2D), one-dimensional (1D) and zero-dimensional (0D), trading spatial

* Corresponding authors.
E-mail addresses: alessandro.brusasco@polito.it (A. Brusasco), mauro.bonfanti@polito.it (M. Bonfanti).

https://doi.org/10.1016/j.ecmx.2026.101527
Received 4 November 2025; Received in revised form 22 December 2025; Accepted 5 January 2026
Available online 9 January 2026
2590-1745/© 2026 The Authors. Published by Elsevier Ltd. This is an open access article under the CC BY license (http://creativecommons.org/licenses/by/4.0/).

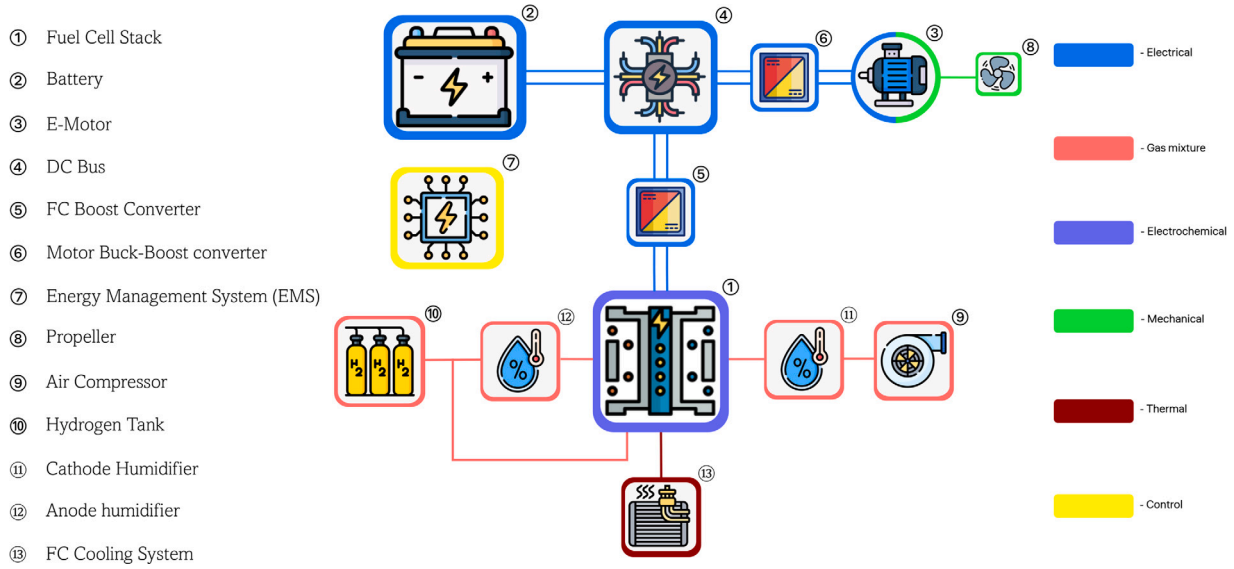

Fig. 1. Propulsion model topology and related domains.

resolution and physical accuracy against computational cost. Computational fluid dynamics (CFD) models capture detailed transport of gases, water and heat in the cell (2D/3D) [10] and are valuable for studying coupled fluid-dynamic and electrochemical processes [11], but their very high computational burden confines their use to off-line analyses [12]. Lower-order 1D models improve efficiency by resolving state evolution along a single coordinate, for instance along the channel direction or through the membrane electrode assembly [9]. There also exist hybrid "3D+1D" or "2D+1D" strategies [13,14], which use higher-fidelity submodels only where needed, but remain too demanding for embedded or real-time applications [15]. For real-time and system-level studies, lumped-parameter 0D models are most suitable. They use spatially averaged variables governed by balance equations and algebraic relations to capture dominant dynamics at low computational cost, at the expense of neglecting spatial gradients [12]. A foundational 0D PEMFC model was proposed by Pukrushpan et al. [16], who decomposed stack behaviour into anode flow, cathode flow, membrane hydration and cell voltage. Subsequent works added physical effects: Hosseinzadeh et al. [17] emphasized water and thermal exchange mechanisms, while Dashti et al. [18] developed a 0D dead-ended anode (DEA) PEMFC stack model to study purge optimization. Since BoP–FC stack interactions strongly affects performance, BoP modelling is crucial at system level. Extensions include coupling the stack with air compressors and anode recirculation [19], or with compressor and back-pressure valve control [20]. Hu et al. [21] further proposed a comprehensive 0D PEMFC system model including humidification dynamics. In hybrid electric powertrains, FCs are usually combined with batteries to handle transient power demands and enhance responsiveness, requiring models of the entire propulsion chain. Several 0D FC–battery powertrain models have been developed. Zecchi et al. [22] proposed a hybrid powertrain model to investigate power split strategies using a simplified electrochemical FC model, while Sun et al. [23] implemented a MATLAB/Simulink model combining a simplified battery with an electrochemical FC model. More comprehensive system-level models exist [24], but often neglect advanced PEMFC dynamic phenomena. Other works use commercial environments such as MATLAB-Simscape for detailed FC–battery powertrain modelling [25], at the cost of reduced computational efficiency.

Based on this review of 0D PEMFC-based powertrain models, two main limitations emerge: high-fidelity FC representations are usually restricted to the stack and BoP, without covering the full propulsion chain, while system-level powertrain models often rely on simplified or empirical FC descriptions, limiting their ability to represent multi-domain dynamics and component couplings. To address this gap, this paper proposes a multi-domain, system-level 0D framework that integrates a detailed PEMFC stack and BoP with a Li-ion battery, power electronics and electric motor. Despite the physical detail, the formulation remains computationally efficient, enabling real-time simulation and making it suitable as a Digital Twin (DT) core for online monitoring and control [26]. The explicit representation of component couplings supports control-oriented applications and Energy Management System (EMS) development [27], including power-split assessment and supervisory control design. The reduced execution time further supports system design and optimization, facilitating extensive parametric studies, virtual prototyping and integration within optimization loops during early-stage powertrain development.

To assess accuracy and computational performance, the proposed model is compared with a functionally equivalent Simscape-based benchmark under realistic maritime load cycles measured on the Vaporetto operating on Venice's Line 1 [28], with data provided by Vulkan Srl. The maritime sector is an attractive application domain for FC–battery powertrains, which are gaining relevance in marine propulsion [29,30]. Venice, heavily reliant on waterborne transport, experiences significant pollutant emissions from its waterbus fleet. Line 1 features a demanding profile, with high-power cruising outside the Canal Grande and low-speed, highly dynamic maneuvering within it, providing a meaningful benchmark to assess the capability of both models to reproduce transient power demands, energy flows and system-level dynamic responses in a real maritime scenario.

The proposed model has been transformed into an open source library, hosted on GitHub [31] and licensed under Creative Commons By Attribution-Share Alike (CC-BY-SA), offering an accessible and customizable tool for both academic and industrial applications.

The structure of this article is as follows. In Section 2, the powertrain components are described. Subsequently, Section 3 focuses on the PEMFC system: starting with a recall of gas mixture dynamics, a high level description is provided for the subcomponents constituting the BoP, as well as the electrochemical and thermodynamic aspects of the FC. In Section 4, the battery model is introduced, while Section 5 describes the model used for the electric motor. Moreover, Section 6 illustrate the components comprising the power conditioning system, followed by an overview of the EMS adopted in this study. Section 7 presents the Simscape model developed to verify the accuracy of the proposed model. In Section 8 are reported the simulation conditions under which the models are tested along with an exhaustive comparison

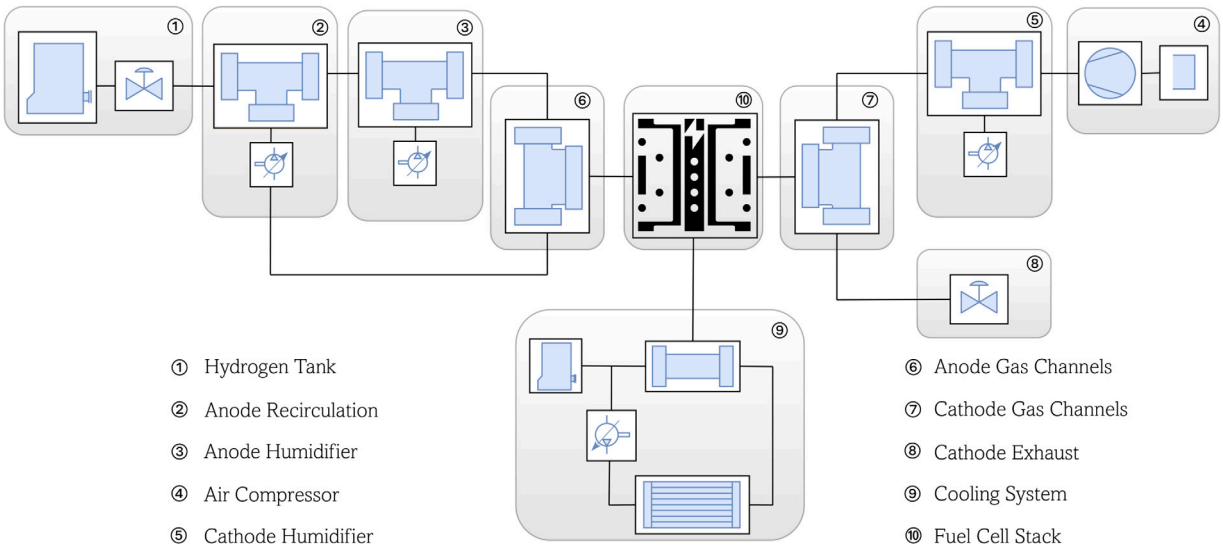

Fig. 2. PEMFC system.

between the two numerical models. In Section 9 the paper concludes with considerations on the obtained results.

2. The electric powertrain

The electric powertrain topology integrates a PEMFC stack and a lithium-ion battery pack in a parallel configuration to drive an electric motor, as shown in Fig. 1. This architecture allows both energy sources to supply the motor simultaneously, providing operational flexibility. During high power demands, the battery supplements the PEMFC output, while under low-load conditions the fuel cell can directly power the motor or recharge the battery. The PEMFC subsystem models the electrochemical, thermodynamic, and gas transport phenomena within the Membrane Electrode Assembly (MEA), together with auxiliary components such as hydrogen storage, air compressor, humidifiers, hydrogen recirculation loop, and cooling system. The battery pack is described through a dynamic model accounting for charge and discharge behaviour. A boost converter regulates the PEMFC output voltage and current according to the EMS commands, while non-zero cable resistances are considered for the wiring. A brushed direct current (DC) motor is adopted, with an electromechanical model and a cascade controller for speed and current regulation. A buck–boost converter ahead of the motor decouples the DC bus from the stator circuit and defines the required terminal voltage. The EMS provides the power split between the PEMFC and the battery, designating the fuel cell as the primary energy source. It is worth emphasizing that all components are embedded within a unified multi-domain state-space model and are not treated as independent black boxes. Subsystems are coupled through energy-conserving connections and shared state variables, while the EMS acts as a supervisory layer providing reference powers and currents without modifying the underlying physical equations.

To facilitate the understanding of the various analytical relationships presented in this study, the variables used have been grouped in Table A.1.

3. PEMFC system

The schematic representation of the PEMFC system is shown in Fig. 2. Hydrogen is supplied from a pressurized tank and regulated by a pressure-reducing valve before being delivered to the anode gas channels. On the cathode side, oxygen is provided by an air compressor. Moisture humidifiers are installed on both anode and cathode sides to maintain appropriate relative humidity levels, thereby minimizing electrochemical losses and ensuring adequate membrane hydration. A hydrogen recirculation loop is implemented on the anode side to redirect unconsumed hydrogen back to the fuel cell, improving fuel utilization. System pressure is regulated by two controllers acting on the hydrogen pressure-reducing valve and the cathode back-pressure valve, respectively. The air compressor is controlled to ensure sufficient oxygen supply and to prevent oxygen starvation. The PEMFC model incorporates the governing equations of gas transport, electrochemical reactions, and thermodynamic processes. A cooling system is included to dissipate the heat generated during operation and to maintain the fuel cell at its optimal operating temperature.

The cathode mixture consists of oxygen, nitrogen, and water vapour, while the anode mixture includes hydrogen, nitrogen, and water vapour. This formulation enables the modelling of nitrogen back-diffusion from the cathode to the anode, which may lead to performance degradation. Although a purge valve is commonly adopted in the anode recirculation loop to mitigate this effect [32], it is neglected in this work for the sake of simplicity. For clarity and completeness, the PEMFC system is described by systematically presenting each component, with particular emphasis on the balance of plant. For each component, the physical inputs and outputs are defined and the governing equations are reported, ensuring transparency, reproducibility, and consistency of the modelling approach. All BoP components are collected in a single comprehensive figure provided in the Appendix (Fig. B.1).

Before presenting the governing equations, the characteristic time scales of the main PEMFC processes are briefly discussed to motivate the adopted modelling assumptions: electrochemical and electrical phenomena typically evolve on microsecond-to-millisecond time scales, whereas gas dynamics occur on the order of seconds and thermal processes on tens to hundreds of seconds. Accordingly, fast processes at the FC electrode level are assumed quasi-instantaneous, while gas and thermal subsystems are modelled dynamically using lumped mass and energy balance equations. This modelling choice represents a deliberate trade-off between physical fidelity and computational efficiency.

3.1. Elements of gas mixture dynamics

To achieve an accurate system-level representation, the dynamic behaviour of the gas mixture within the anode and cathode networks is explicitly modelled using lumped mass balance equations. Each component is treated as either a pipe or a chamber, where the gas

mixture dynamics are explicitly formulated to capture transient effects and system interactions. A set of fundamental assumptions is adopted: (i) perfectly rigid pipe walls, ensuring no structural deformation; (ii) negligible friction losses, assuming smooth internal surfaces; (iii) subsonic flow conditions; (iv) negligible fluid inertia; and (v) the absence of gravitational effects. From here on, subscripts a, w, and g indicate the properties of dry air, water vapour, and trace gas, respectively. Moreover, a positive flow rate denotes inflow into the pipe, whereas a negative value represents outflow.

3.1.1. Gas mixture dynamics equations

Considering a moisture flow passing through a rigid pipe or chamber, the mass and energy conservation governing the gas mixture dynamics can be formulated as follows [33]:

$$\frac{dm}{dt} = \dot{m}_{\text{in}} - \dot{m}_{\text{out}} - \dot{m}_{\text{cond}}, \tag{1a}$$

$$\frac{d\boldsymbol{\Phi}}{dt} = \boldsymbol{\Phi}_{\text{in}} - \boldsymbol{\Phi}_{\text{out}} - \boldsymbol{\Phi}_{\text{cond}} + Q, \tag{1b}$$

$$\frac{dm_w}{dt} = \dot{m}_{\text{w,in}} - \dot{m}_{\text{w,out}} - \dot{m}_{\text{cond}}, \tag{1c}$$

$$\frac{dm_g}{dt} = \dot{m}_{\text{g,in}} - \dot{m}_{\text{g,out}}. \tag{1d}$$

The mass balance (Eq. (1a)) considers the inlet and outlet mass flow rates, ($\dot{m}_{\text{in}}$ and $\dot{m}_{\text{out}}$ respectively), while it accounts also for the rate of water condensation ($\dot{m}_{\text{cond}}$). The energy balance (Eq. (1b)) accounts for the net energy flux ($\boldsymbol{\Phi}_{\text{in}} - \boldsymbol{\Phi}_{\text{out}}$), the energy loss due to condensation ($\boldsymbol{\Phi}_{\text{cond}}$), and the heat exchange (Q) between the pipe wall and the internal gas volume. The mass balance of individual gas species (Eqs. (1c) and (1d)) follows the same principles, with $\dot{m}_{\text{w,in}}$ and $\dot{m}_{\text{w,out}}$ representing the water mass inflow and outflow, respectively, while $\dot{m}_{\text{g,in}}$ and $\dot{m}_{\text{g,out}}$ correspond to the inlet and outlet flow rates of gas species.

To determine the outlet flow rate of the pipe, the nozzle flow equations are applied. Depending on the pressure ratio across the nozzle, the flow can either be choked or unchoked [34]. In the choked flow regime, the velocity at the nozzle throat reaches the speed of sound, limiting the maximum possible flow rate. Conversely, in the unchoked regime, the flow rate remains pressure-dependent, governed by subsonic conditions. Therefore, if the pressure ratio is small, the flow is subcritical and can be linearized as follows [16]:

$$\dot{m}_{\text{out}} = k_{\text{f}}(p_{\text{I}} - p_{\text{out}}), \tag{2}$$

where k_{f} is the nozzle constant, p_{I} is the pipe internal pressure and p_{out} is the downstream pressure.

The energy flow associated to the mixture is defined exploiting the definition of total enthalpy, as:

$$\boldsymbol{\Phi}_{\text{out}} = \dot{m}_{\text{out}} \left(h_{\text{I}} + \frac{1}{2} \left(\frac{\dot{m}_{\text{out}}}{\rho_{\text{I}} S_{\text{p}}} \right)^2 \right), \tag{3}$$

where S_{p} is the pipe cross-sectional area and ρ_{I} is the mixture internal density. h_{I} is the mixture specific enthalpy, calculated as follows:

$$h_{\text{I}} = x_{\text{a}} h_{\text{a}} + x_{\text{g}} h_{\text{g}} + x_{\text{w}} h_{\text{w}}, \tag{4}$$

where letters x indicate the mass fraction of a specific species, and $x_{\text{a}} + x_{\text{g}} + x_{\text{w}} = 1$. The dynamics of the mass fraction of each mixture component is:

$$\frac{dx}{dt}\rho_{\text{I}} V_{\text{p}} + x\frac{dm}{dt} = \frac{d(xm)}{dt}, \tag{5}$$

where V_{p} is the internal volume of the pipe. Then, the mixture pressure and temperature dynamics equations are reported in Eqs. (6a) and (6b) (see Box I) [33].

In Eq. (6), T_{I} is the mixture temperature, R_{I} is the mixture specific gas constant, $c_{\text{v,I}}$ is the mixture specific heat at constant volume, and u_{I} the specific internal energy. R_{I}, $c_{\text{v,I}}$, and u_{I} are defined as follows:

$$R_{\text{I}} = x_{\text{a}} R_{\text{a}} + x_{\text{g}} R_{\text{g}} + x_{\text{w}} R_{\text{w}}, \tag{7a}$$

$$c_{\text{v,I}} = x_{\text{a}} c_{\text{va,}} + x_{\text{g}} c_{\text{v,g}} + x_{\text{w}} c_{\text{v,w}}, \tag{7b}$$

$$u_{\text{I}} = x_{\text{a}} u_{\text{a}} + x_{\text{g}} u_{\text{g}} + x_{\text{w}} u_{\text{w}}. \tag{7c}$$

Then, the equation of state relates the mixture density to the pressure and temperature, as follows:

$$p_{\text{I}} = \rho_{\text{I}} R_{\text{I}} T_{\text{I}}. \tag{8}$$

3.1.2. Condensation and wall heat transfer

In Eq. (1b) appears the term related to the heat exchange (Q) between the fluid and the wall of the pipe. It is given by both convective and conductive contributions, as follows:

$$Q = Q_{\text{conv}} + Q_{\text{cond}}. \tag{9}$$

The convective term is defined as follows [35]:

$$Q_{\text{cond}} = \frac{k_{\text{I}} S_{\text{surf}}}{D_{\text{h}}} (T_{\text{w}} - T_{\text{I}}), \tag{10}$$

in which k_{I} is the mixture thermal conductivity, T_{w} is the temperature of pipe walls, D_{h} is the hydraulic diameter of the pipe and S_{surf} is the pipe surface area. As it is assumed an exponential distribution of the temperature along the pipe, the conductive heat exchange Q_{conv} can be defined as [35]:

$$Q_{\text{conv}} = |\dot{m}_{\text{avg}}| c_{\text{p,avg}} (T_{\text{w}} - T_{\text{in}}) \left(1 - \text{e}^{-\frac{h S_{\text{surf}}}{|\dot{m}_{\text{avg}}| c_{\text{p,avg}}}} \right), \tag{11}$$

where T_{in} is the inlet mixture temperature according to the flow direction, $\dot{m}_{\text{avg}}$ is the average mass flow rate between inlet and outlet, and $c_{\text{p,avg}}$ is the average mixture specific heat between inlet and outlet. The term h is the heat transfer coefficient:

$$h = N_{\text{u}} k_{\text{avg}} / D_{\text{h}}, \tag{12}$$

where k_{avg} is the average mixture thermal conductivity between inlet and outlet. N_{u} is the Nusselt number, that for a laminar flow is constant, whereas for turbulent flow is defined using the Gnielinski's correlation [36]. Finally, the equations that account for water condensation on pipe walls follow:

$$\dot{m}_{\text{cond}} = \begin{cases} 0 & \text{if } x_{\text{w}} \leq x_{\text{ws}} \\ \frac{x_{\text{w}} - x_{\text{ws}}}{\tau_{\text{cond}}} \rho_{\text{I}} V_{\text{p}} & \text{if } x_{\text{w}} > x_{\text{ws}} \end{cases}, \tag{13}$$

where τ_{cond} is the condensation time constant and x_{ws} is defined as the specific humidity at saturation:

$$x_{\text{ws}} = \phi_{\text{ws}} \frac{R_{\text{I}}}{R_{\text{w}}} \frac{p_{\text{ws}}}{p_{\text{I}}}, \tag{14}$$

in which ϕ_{ws} is the relative humidity at saturation, equal to 1, and p_{ws} is the water saturation pressure evaluated at the pipe temperature. The energy loss associated to the condensed water vapour is:

$$\boldsymbol{\Phi}_{\text{cond}} = \dot{m}_{\text{cond}} (h_{\text{w}} - \Delta h_{\text{vap}}), \tag{15}$$

where Δh_{vap} is the water specific enthalpy of vaporization evaluated at the pipe temperature.

In some system components, the effects of wall heat transfer and water vapour condensation can be considered negligible, as they do not significantly affect the dynamics of the gas mixture. Hence, additional simplifying assumptions are introduced to reduce the overall computational burden of the model. These assumptions help streamline the simulation while maintaining accuracy in the key dynamic behaviour. A summary of these assumptions is provided in Table 3.1 and will be further detailed for each component.

$$\rho_{\mathrm{I}} V_{\mathrm{p}} \left(\frac{dp_{\mathrm{I}}}{dt} \frac{1}{p_{\mathrm{I}}} - \frac{dT_{\mathrm{I}}}{dt} \frac{1}{T_{\mathrm{I}}} \right) = \frac{dm}{dt} - \frac{R_{\mathrm{a}} - R_{\mathrm{w}}}{R_{\mathrm{I}}} \left(\frac{dm_{\mathrm{w}}}{dt} - x_{\mathrm{w}} \frac{dm}{dt} \right) - \frac{R_{\mathrm{a}} - R_{\mathrm{g}}}{R_{\mathrm{I}}} \left(\frac{dm_{\mathrm{g}}}{dt} - x_{\mathrm{g}} \frac{dm}{dt} \right), \tag{6a}$$

$$\rho_{\mathrm{I}} c_{\mathrm{v,I}} V_{\mathrm{p}} \frac{dT_{\mathrm{I}}}{dt} = \frac{d\boldsymbol{\Phi}}{dt} - (u_{\mathrm{w}} - u_{\mathrm{a}}) \left(\frac{dm_{\mathrm{w}}}{dt} - x_{\mathrm{w}} \frac{dm}{dt} \right) + (u_{\mathrm{g}} - u_{\mathrm{a}}) \left(\frac{dm_{\mathrm{g}}}{dt} - x_{\mathrm{g}} \frac{dm}{dt} \right) - u_{\mathrm{I}} \frac{dm}{dt}. \tag{6b}$$

Box I.

Table 3.1
Additional assumptions on each balance of plant component. ✓: Considered, x: Neglected.

Component	Heat transfer	Condensation effect
Hydrogen tank	x	x
Recirculation	x	✓
Anode humidifier	x	✓
Anode gas channels	✓	✓
Cathode gas channels	✓	✓
Cathode humidifier	x	✓
Air compressor	x	x

3.2. Hydrogen tank

The hydrogen, that is stored into a pressurized tank, is modelled as a fixed volume chamber with one outlet. The chamber is considered thermally insulated and it is assumed that pure hydrogen is stocked ($x_{\mathrm{g}} = 1$ holds, where $g = H_2$), thus the condensation effect is neglected and the hydrogen does not exchange heat with the environment. As a consequence, the hydrogen dynamics equations follow:

$$\frac{dm_{\mathrm{t}}}{dt} = -\dot{m}_{\mathrm{out,t}}, \tag{16a}$$

$$\frac{d\boldsymbol{\Phi}_{\mathrm{t}}}{dt} = -\boldsymbol{\Phi}_{\mathrm{out,t}}. \tag{16b}$$

Then, the pressure and temperature dynamics equations are defined as:

$$\rho_{\mathrm{I,t}} V_{\mathrm{t}} \left(\frac{dp_{\mathrm{I,t}}}{dt} \frac{1}{p_{\mathrm{I,t}}} - \frac{dT_{\mathrm{I,t}}}{dt} \frac{1}{T_{\mathrm{I,t}}} \right) = \frac{dm_{\mathrm{t}}}{dt}, \tag{17a}$$

$$\rho_{\mathrm{I,t}} c_{\mathrm{v,I}} V_{\mathrm{t}} \frac{dT_{\mathrm{I,t}}}{dt} = \frac{d\boldsymbol{\Phi}_{\mathrm{t}}}{dt} - u_{\mathrm{I}} \frac{dm_{\mathrm{t}}}{dt}. \tag{17b}$$

The hydrogen flow is controlled by a valve, that is activated by a proportional control algorithm, ensuring that the pressure inside the anode networks is kept around a predefined reference value. The controller sets the valve opening as:

$$S_{\mathrm{v,t}}^{\mathrm{des}} = k_{\mathrm{p,vt}} (p_{\mathrm{I,r}} - p_{\mathrm{anode}}^{\mathrm{ref}}), \tag{18}$$

in which $S_{\mathrm{v,t}}^{\mathrm{des}}$ is the desired cross-sectional area of the valve, $k_{\mathrm{p,vt}}$ is the proportional control gain, $p_{\mathrm{I,r}}$ is the pressure at the valve outlet and $p_{\mathrm{anode}}^{\mathrm{ref}}$ is the anode network reference pressure. Thus, the outlet flow rate $\dot{m}_{\mathrm{out,t}}$ is defined as follows:

$$\dot{m}_{\mathrm{out,t}} = k_{\mathrm{v,t}} C_{\mathrm{d,t}} S_{\mathrm{v,t}}^{\mathrm{des}} \sqrt{2\rho_{\mathrm{I,t}} (p_{\mathrm{I,t}} - p_{\mathrm{I,r}})}, \tag{19}$$

in which $C_{\mathrm{d,t}}$ is the tank discharge coefficient and $k_{\mathrm{v,t}}$ is a modulating coefficient defined as:

$$k_{\mathrm{v,t}} = \tanh \left(k'_{\mathrm{v,t}} \sqrt{2\rho_{\mathrm{I,t}} (p_{\mathrm{I,t}} - p_{\mathrm{I,r}})} \right), \tag{20}$$

where $k'_{\mathrm{v,t}}$ is an arbitrary coefficient. This correction to the outlet mass flow rate allows the flow to be modulated in such a way that, given the very high pressure difference, it can represent the physical effect of choking. To prevent a negative opening of the valve, $S_{\mathrm{v,t}}^{\mathrm{des}}$ is saturated to a minimum positive threshold.

3.3. Anode recirculation

Here, the hydrogen flow coming from the tank blends with the gas mixture exiting form the FC. The flow coming from the anode gas channel is driven by an ideal blower, that does not add or remove energy to the flow. The recirculation is modelled as a three inlet chamber that is thermally insulated. Thus, the gas dynamics equations are:

$$\frac{dm_{\mathrm{r}}}{dt} = \dot{m}_{\mathrm{out,t}} + \dot{m}_{\mathrm{out,a}} - \dot{m}_{\mathrm{out,r}} - \dot{m}_{\mathrm{cond,r}}, \tag{21a}$$

$$\frac{d\boldsymbol{\Phi}_{\mathrm{r}}}{dt} = \boldsymbol{\Phi}_{\mathrm{out,t}} + \boldsymbol{\Phi}_{\mathrm{out,a}} - \boldsymbol{\Phi}_{\mathrm{out,r}} - \boldsymbol{\Phi}_{\mathrm{cond,r}}, \tag{21b}$$

$$\frac{dm_{\mathrm{H_2O,r}}}{dt} = \dot{m}_{\mathrm{H_2O,out,a}} - \dot{m}_{\mathrm{H_2O,out,r}} - \dot{m}_{\mathrm{cond,r}}, \tag{21c}$$

$$\frac{dm_{\mathrm{H_2,r}}}{dt} = \dot{m}_{\mathrm{out,t}} + \dot{m}_{\mathrm{H_2,out,a}} - \dot{m}_{\mathrm{H_2,out,r}}. \tag{21d}$$

The outlet mass flow rate $\dot{m}_{\mathrm{out,r}}$ and the outlet energy flow rate $\boldsymbol{\Phi}_{\mathrm{out,r}}$ are defined as follows:

$$\dot{m}_{\mathrm{out,r}} = k_{\mathrm{f,r}} (p_{\mathrm{I,r}} - p_{\mathrm{I,ha}}), \tag{22a}$$

$$\boldsymbol{\Phi}_{\mathrm{out,r}} = \dot{m}_{\mathrm{out,r}} \left(h_{\mathrm{I}} + \frac{1}{2} \left(\frac{\dot{m}_{\mathrm{out,r}}}{\rho_{\mathrm{I,r}} S_{\mathrm{r}}} \right)^2 \right), \tag{22b}$$

where $p_{\mathrm{I,ha}}$ is the anode humidifier pressure. $\dot{m}_{\mathrm{out,a}}$, $\dot{m}_{\mathrm{H_2,out,a}}$, $\dot{m}_{\mathrm{H_2O,out,a}}$ and $\boldsymbol{\Phi}_{\mathrm{out,a}}$ are the flow rates exiting the anode gas channels and driven from the ideal blower up to the recirculation chamber. The blower is controlled by a proportional law that define the desired flow rate $\dot{m}_{\mathrm{out,a}}^{\mathrm{ref}}$ according to the value of the current flowing into the FC (I_{FC}), as follows:

$$\dot{m}_{\mathrm{out,a}} = \dot{m}_{\mathrm{out,a}}^{\mathrm{ref}} = k'_{\mathrm{p,r}} (c_{\mathrm{r}} + k_{\mathrm{p,r}} I_{\mathrm{FC}}), \tag{23}$$

in which c_{r} is an adding constant, $k_{\mathrm{p,r}}$ and $k'_{\mathrm{p,r}}$ are the control proportional gains. The adding constant allows a minimum recirculation flow even at zero current. The dynamics of temperature and pressure are reported in Eqs. (24a) and (24b)(see Box II).

3.4. Anode humidifier

The humidifier is modelled as a three inlet pipe, in which the water vapour is injected into the pipe flow through an ideal moisture source. The pipe is assumed insulated from the environment, thus the governing gas dynamics equations are:

$$\frac{dm_{\mathrm{ha}}}{dt} = \dot{m}_{\mathrm{out,r}} + \dot{m}_{\mathrm{inj,ha}} - \dot{m}_{\mathrm{out,ha}} - \dot{m}_{\mathrm{cond,ha}}, \tag{25a}$$

$$\frac{d\boldsymbol{\Phi}_{\mathrm{ha}}}{dt} = \boldsymbol{\Phi}_{\mathrm{out,r}} + \boldsymbol{\Phi}_{\mathrm{inj,ha}} - \boldsymbol{\Phi}_{\mathrm{out,ha}} - \boldsymbol{\Phi}_{\mathrm{cond,ha}}, \tag{25b}$$

$$\frac{dm_{\mathrm{H_2O,ha}}}{dt} = \dot{m}_{\mathrm{H_2O,out,r}} + \dot{m}_{\mathrm{inj,ha}} - \dot{m}_{\mathrm{H_2O,out,ha}} - \dot{m}_{\mathrm{cond,ha}}, \tag{25c}$$

$$\frac{dm_{\mathrm{H_2,ha}}}{dt} = \dot{m}_{\mathrm{H_2,out,r}} - \dot{m}_{\mathrm{H_2,out,ha}}. \tag{25d}$$

$$\rho_{\mathrm{I,r}} V_{\mathrm{r}} \left(\frac{dp_{\mathrm{I,r}}}{dt} \frac{1}{p_{\mathrm{I,r}}} - \frac{dT_{\mathrm{I,r}}}{dt} \frac{1}{T_{\mathrm{I,r}}} \right) = \frac{dm_{\mathrm{r}}}{dt} - \frac{R_{\mathrm{N_2}} - R_{\mathrm{H_2O}}}{R_{\mathrm{I}}} \left(\frac{dm_{\mathrm{H_2O,r}}}{dt} - x_{\mathrm{H_2O}} \frac{dm_{\mathrm{r}}}{dt} \right) - \frac{R_{\mathrm{N_2}} - R_{\mathrm{H_2}}}{R_{\mathrm{I}}} \left(\frac{dm_{\mathrm{H_2,r}}}{dt} - x_{\mathrm{H_2}} \frac{dm_{\mathrm{r}}}{dt} \right), \tag{24a}$$

$$\rho_{\mathrm{I,r}} c_{\mathrm{v,I}} V_{\mathrm{r}} \frac{dT_{\mathrm{I,r}}}{dt} = \frac{d\Phi_{\mathrm{r}}}{dt} - (u_{\mathrm{H_2O}} - u_{\mathrm{N_2}}) \left(\frac{dm_{\mathrm{H_2O,r}}}{dt} - x_{\mathrm{H_2O}} \frac{dm_{\mathrm{r}}}{dt} \right) + (u_{\mathrm{H_2}} - u_{\mathrm{N_2}}) \left(\frac{dm_{\mathrm{H_2,r}}}{dt} - x_{\mathrm{H_2}} \frac{dm_{\mathrm{r}}}{dt} \right) - u_{\mathrm{I}} \frac{dm_{\mathrm{r}}}{dt}. \tag{24b}$$

Box II.

$$\rho_{\mathrm{I,ha}} V_{\mathrm{ha}} \left(\frac{dp_{\mathrm{I,ha}}}{dt} \frac{1}{p_{\mathrm{I,ha}}} - \frac{dT_{\mathrm{I,ha}}}{dt} \frac{1}{T_{\mathrm{I,ha}}} \right) = \frac{dm_{\mathrm{ha}}}{dt} - \frac{R_{\mathrm{N_2}} - R_{\mathrm{H_2O}}}{R_{\mathrm{I}}} \left(\frac{dm_{\mathrm{H_2O,ha}}}{dt} - x_{\mathrm{H_2O}} \frac{dm_{\mathrm{ha}}}{dt} \right) - \frac{R_{\mathrm{N_2}} - R_{\mathrm{H_2}}}{R_{\mathrm{I}}} \left(\frac{dm_{\mathrm{H_2,ha}}}{dt} - x_{\mathrm{H_2}} \frac{dm_{\mathrm{ha}}}{dt} \right), \tag{26a}$$

$$\rho_{\mathrm{I,ha}} c_{\mathrm{v,I}} V_{\mathrm{ha}} \frac{dT_{\mathrm{I,ha}}}{dt} = \frac{d\Phi_{\mathrm{ha}}}{dt} - (u_{\mathrm{H_2O}} - u_{\mathrm{N_2}}) \left(\frac{dm_{\mathrm{H_2O,ha}}}{dt} - x_{\mathrm{H_2O}} \frac{dm_{\mathrm{ha}}}{dt} \right) + (u_{\mathrm{H_2}} - u_{\mathrm{N_2}}) \left(\frac{dm_{\mathrm{H_2,ha}}}{dt} - x_{\mathrm{H_2}} \frac{dm_{\mathrm{ha}}}{dt} \right) - u_{\mathrm{I}} \frac{dm_{\mathrm{ha}}}{dt}. \tag{26b}$$

Box III.

Then, the pressure and temperature dynamics equations are reported in Eqs. (26a) and (26b)(see Box III). The outlet mass flow rate $\dot{m}_{\mathrm{out,ha}}$ and the outlet energy flow rate $\Phi_{\mathrm{out,ha}}$ are evaluated through the following equations:

$$\dot{m}_{\mathrm{out,ha}} = k_{\mathrm{f,ha}} (p_{\mathrm{I,ha}} - p_{\mathrm{I,a}}), \tag{27a}$$

$$\Phi_{\mathrm{out,ha}} = \dot{m}_{\mathrm{out,ha}} \left(h_{\mathrm{I}} + \frac{1}{2} \left(\frac{\dot{m}_{\mathrm{out,ha}}}{\rho_{\mathrm{I,ha}} S_{\mathrm{ha}}} \right)^2 \right), \tag{27b}$$

where $p_{\mathrm{I,a}}$ is the anode gas channels pressure. The moisture source injects water vapour through a proportional control logic, that defines the reference injected water vapour flow rate $\dot{m}^{\mathrm{ref}}_{\mathrm{inj,ha}}$ that allows to reach the relative humidity setpoint RH_{set}. As ideal conditions are considered, the reference flow rate is equal to the actual one, as follows:

$$\dot{m}_{\mathrm{inj,ha}} = \dot{m}^{\mathrm{ref}}_{\mathrm{inj,ha}} = k_{\mathrm{p,ha}} (RH_{\mathrm{set}} - RH_{\mathrm{I,ha}}), \tag{28}$$

where $RH_{\mathrm{I,ha}}$ is the measured relative humidity in the pipe and $k_{\mathrm{p,ha}}$ is the proportional control gain. The energy of water vapour injected is:

$$\Phi_{\mathrm{inj,ha}} = \dot{m}_{\mathrm{inj,ha}} h_{\mathrm{H_2O}}. \tag{29}$$

The water specific enthalpy h_{H2O} is evaluated at the temperature of the FC, since it is assumed that the water produced by the fuel cell is reused for the humidification.

In the simulations reported in Section 8, the relative humidity setpoint is fixed at 100 % for both anode and cathode, reflecting the common design objective of delivering fully humidified reactants at the stack inlet and enabling the analysis of potential flooding conditions. The model formulation, however, allows for arbitrary humidity setpoints by adjusting RH_{set}.

3.5. Air compressor

The air compressor is modelled using a 3D performance map that defines the air mass flow rate as a function of the compressor rotational speed and of the pressure ratio between outlet and inlet. The map can be replaced by any other compressor map expressed in the same variables, thus preserving the generality of the underlying formulation. The air flow rate is imposed through an ideal flow source that draws air from the environment and delivers it to a downstream chamber, in which gas dynamics is formulated. The outlet air temperature is computed from an energy balance based on mass flow rate, pressure ratio, and compressor isentropic efficiency, thereby accounting for the dominant temperature rise due to compression; additional thermal and mechanical losses are assumed to have a second order effect within the operating range considered. Wall heat transfer, condensation effects, and mechanical heat dissipation are neglected. The rotational inertia of the compressor shaft, as well as surge and stall phenomena, are not explicitly modelled. All these effects are therefore considered as a simplifying assumption. Finally, a control algorithm regulates the compressor operating point in accordance with the fuel cell power request.

The gas mixture dynamics equations are formulated as follows:

$$\frac{dm_{\mathrm{cp}}}{dt} = \dot{m}_{\mathrm{in,cp}} - \dot{m}_{\mathrm{out,cp}}, \tag{30a}$$

$$\frac{d\Phi_{\mathrm{cp}}}{dt} = \Phi_{\mathrm{in,cp}} - \Phi_{\mathrm{out,cp}}, \tag{30b}$$

$$\frac{dm_{\mathrm{H_2O,cp}}}{dt} = \dot{m}_{\mathrm{H_2O,in,cp}} - \dot{m}_{\mathrm{H_2O,out,cp}}, \tag{30c}$$

$$\frac{dm_{\mathrm{O_2,cp}}}{dt} = \dot{m}_{\mathrm{O_2,in,cp}} - \dot{m}_{\mathrm{O_2,out,cp}}. \tag{30d}$$

Subsequently, the pressure and temperature dynamics equations are retrieved, as shown in the Eqs. (31a) and (31b)(see Box IV).

The outlet mass and energy flow rate are evaluated as follows:

$$\dot{m}_{\mathrm{out,cp}} = k_{\mathrm{f,cp}} (p_{\mathrm{I,cp}} - p_{\mathrm{I,hc}}), \tag{32a}$$

$$\Phi_{\mathrm{out,cp}} = \dot{m}_{\mathrm{out,cp}} \left(h_{\mathrm{I}} + \frac{1}{2} \left(\frac{\dot{m}_{\mathrm{out,cp}}}{\rho_{\mathrm{I,cp}} S_{\mathrm{cp,out}}} \right)^2 \right), \tag{32b}$$

where $p_{\mathrm{I,hc}}$ is the cathode humidifier pressure and $S_{\mathrm{cp,out}}$ is the compressor outlet cross-sectional area. $\dot{m}_{\mathrm{in,cp}}$ is evaluated exploiting the corrected mass flow rate $\dot{m}_{\mathrm{corr}}$, as follows [37]:

$$m_{\mathrm{in,cp}} = \dot{m}_{\mathrm{corr}} \frac{p_{\mathrm{in,cp}}}{p_{\mathrm{env}}} \sqrt{\frac{T_{\mathrm{env}}}{T_{\mathrm{in,cp}}}}, \tag{33}$$

in which $p_{\mathrm{in,cp}}$ and $T_{\mathrm{in,cp}}$ are respectively the pressure and temperature at the compressor inlet, while p_{env} and T_{env} are environment pressure and temperature. $\dot{m}_{\mathrm{corr}}$ is retrieved by means of the compressor 3D map as a function of the ratio of pressure between outlet and inlet (p_{ratio}) and the reference rotational speed of the compressor ($\omega^{\mathrm{ref}}_{\mathrm{cp}}$), defined by the compressor control. The compressor map has been constructed by defining a vector of pressure ratios $p^{\mathrm{LUT}}_{\mathrm{ratio}} = [p_1\ p_2\ p_3\ p_4\ p_5]^T$ and a vector of compressor rotational speeds $\omega^{\mathrm{LUT}}_{\mathrm{cp}} = [\omega_1\ \omega_2\ \omega_3]$. For each pair of points $(p_i,\ \omega_j)$ there is a corresponding value of corrected flow rate m_{ij}, which is arranged in a 5 × 3 matrix, $\dot{m}^{\mathrm{LUT}}_{\mathrm{corr}}$. The corrected mass flow

$$\rho_{\mathrm{I,cp}} V_{\mathrm{cp}} \left(\frac{dp_{\mathrm{I,cp}}}{dt} \frac{1}{p_{\mathrm{I,cp}}} - \frac{dT_{\mathrm{I,cp}}}{dt} \frac{1}{T_{\mathrm{I,cp}}} \right) = \frac{dm_{\mathrm{cp}}}{dt} - \frac{R_{\mathrm{N_2}} - R_{\mathrm{H_2O}}}{R_{\mathrm{I}}} \left(\frac{dm_{\mathrm{H_2O,cp}}}{dt} - x_{\mathrm{H_2O}} \frac{dm_{\mathrm{cp}}}{dt} \right) - \frac{R_{\mathrm{N_2}} - R_{\mathrm{O_2}}}{R_{\mathrm{I}}} \left(\frac{dm_{\mathrm{O_2,cp}}}{dt} - x_{\mathrm{O_2}} \frac{dm_{\mathrm{cp}}}{dt} \right), \tag{31a}$$

$$\rho_{\mathrm{I,cp}} c_{\mathrm{v,I}} V_{\mathrm{cp}} \frac{dT_{\mathrm{I,cp}}}{dt} = \frac{d\Phi_{\mathrm{cp}}}{dt} - (u_{\mathrm{H_2O}} - u_{\mathrm{N_2}}) \left(\frac{dm_{\mathrm{H_2O,cp}}}{dt} - x_{\mathrm{H_2O}} \frac{dm_{\mathrm{cp}}}{dt} \right) + (u_{\mathrm{H_2}} - u_{\mathrm{N_2}}) \left(\frac{dm_{\mathrm{O_2,cp}}}{dt} - x_{\mathrm{O_2}} \frac{dm_{\mathrm{cp}}}{dt} \right) - u_{\mathrm{I}} \frac{dm_{\mathrm{cp}}}{dt}. \tag{31b}$$

Box IV.

rate $\dot{m}_{\mathrm{corr}}$ is computed at each simulation step by means of a bilinear interpolation over the two vectors.

As the FC must always have an adequate supply of oxygen, a Proportional-Integral (PI) control law is implemented to ensure that the following reference air flow rate is always provided by the air compressor:

$$\dot{m}^{\mathrm{ref}}_{\mathrm{in,cp}} = \frac{\lambda_{\mathrm{O_2}} \dot{m}^{\mathrm{ref}}_{\mathrm{O_2,cons}}}{x_{\mathrm{O_2,env}}}, \tag{34}$$

where $x_{\mathrm{O_2,env}}$ is the environmental oxygen mass fraction and $\dot{m}^{\mathrm{ref}}_{\mathrm{O_2,cons}}$ is the oxygen rate of consumption, evaluated from the reference FC current $I^{\mathrm{ref}}_{\mathrm{FC}}$ (that is defined by the EMS) as follows [38]:

$$\dot{m}^{\mathrm{ref}}_{\mathrm{O_2,cons}} = N_{\mathrm{c}} M_{\mathrm{O_2}} \frac{I^{\mathrm{ref}}_{\mathrm{FC}}}{4F}, \tag{35}$$

where N_{c} is the number of cell in the FC, $M_{\mathrm{O_2}}$ is the oxygen molar mass, and F is the Faraday's constant. In Eq. (34) appears $\lambda_{\mathrm{O_2}}$, the Oxygen Excess Ratio (OER), that is the ratio between the oxygen flow rate entering the cathode and the oxygen rate of consumption [39]. The output of the PI controller is the command that defines the reference rotational speed of the compressor $\omega^{\mathrm{ref}}_{\mathrm{cp}}$ as follows:

$$\omega^{\mathrm{ref}}_{\mathrm{cp}} = \omega_{\mathrm{cp,max}} k_{\mathrm{P,cp}} \left((\dot{m}^{\mathrm{ref}}_{\mathrm{in,cp}} - \dot{m}_{\mathrm{out,cp}}) + k_{\mathrm{I,cp}} \int_0^t (\dot{m}^{\mathrm{ref}}_{\mathrm{in,cp}} - \dot{m}_{\mathrm{out,cp}}) dt \right) \tag{36}$$

where $k_{\mathrm{P,cp}}$ and $k_{\mathrm{I,cp}}$ are respectively the proportional and integral control gain of the compressor control and $\omega_{\mathrm{cp,max}}$ is the compressor maximum rotational velocity. Back to Eq. (30b), the term $\Phi_{\mathrm{in,cp}}$ is the compressor pipe inlet energy flow rate, defined as:

$$\Phi_{\mathrm{in,cp}} = \dot{m}_{\mathrm{in,cp}} h_{\mathrm{T,in}} + \Phi_{\mathrm{work,cp}}, \tag{37}$$

where $\Phi_{\mathrm{work,cp}}$ is power spent by the compressor, modelled as isentropic [33]:

$$\Phi_{\mathrm{work,cp}} = \dot{m}_{\mathrm{in,cp}} (h_{\mathrm{T,in}} - h_{\mathrm{T,out}}), \tag{38}$$

where

$$h_{\mathrm{T,in}} = h_{\mathrm{env}} + \frac{1}{2} \left(\frac{\dot{m}_{\mathrm{in,cp}}}{\rho_{\mathrm{env}} S_{\mathrm{cp,in}}} \right)^2, \tag{39a}$$

$$h_{\mathrm{T,out}} = h_{\mathrm{I}} + \frac{1}{2} \left(\frac{\dot{m}_{\mathrm{out,cp}}}{\rho_{\mathrm{I,cp}} S_{\mathrm{cp,out}}} \right)^2, \tag{39b}$$

in which $S_{\mathrm{cp,in}}$ is the compressor inlet cross-sectional area, h_{env}, ρ_{env} are respectively the specific enthalpy and density of air in environmental conditions, and $h_{\mathrm{T,in}}$ and $h_{\mathrm{T,out}}$ are the total enthalpies at the compressor inlet and outlet, respectively.

3.6. Cathode humidifier

The cathode humidifier is modelled as a pipe with three inlets. Water vapour is introduced into the flow through a ideal moisture source. The pipe is considered to be thermally insulated, thus the dynamic equations of gas mixture are:

$$\frac{dm_{\mathrm{hc}}}{dt} = \dot{m}_{\mathrm{out,cp}} + \dot{m}_{\mathrm{inj,hc}} - \dot{m}_{\mathrm{out,hc}} - \dot{m}_{\mathrm{cond,hc}}, \tag{40a}$$

$$\frac{d\Phi_{\mathrm{hc}}}{dt} = \Phi_{\mathrm{out,cp}} + \Phi_{\mathrm{inj,hc}} - \Phi_{\mathrm{out,hc}} - \Phi_{\mathrm{cond,hc}}, \tag{40b}$$

$$\frac{dm_{\mathrm{H_2O,hc}}}{dt} = \dot{m}_{\mathrm{H_2O,out,cp}} + \dot{m}_{\mathrm{inj,hc}} - \dot{m}_{\mathrm{H_2O,out,hc}} - \dot{m}_{\mathrm{cond,hc}}, \tag{40c}$$

$$\frac{dm_{\mathrm{O_2,hc}}}{dt} = \dot{m}_{\mathrm{O_2,out,cp}} - \dot{m}_{\mathrm{O_2,out,hc}}. \tag{40d}$$

Subsequently, the pressure and temperature dynamics equations are retrieved in Eqs. (41a) and (41b)(see Box V).

The outlet mass flow rate $\dot{m}_{\mathrm{out,hc}}$ and the outlet energy flow rate $\Phi_{\mathrm{out,hc}}$ are calculated using the following equations:

$$\dot{m}_{\mathrm{out,hc}} = k_{\mathrm{f,hc}} (p_{\mathrm{I,hc}} - p_{\mathrm{I,c}}), \tag{42a}$$

$$\Phi_{\mathrm{out,hc}} = \dot{m}_{\mathrm{out,hc}} \left(h_{\mathrm{I}} + \frac{1}{2} \left(\frac{\dot{m}_{\mathrm{out,hc}}}{\rho_{\mathrm{I,hc}} S_{\mathrm{hc}}} \right)^2 \right), \tag{42b}$$

where $p_{\mathrm{I,c}}$ is the cathode gas channels pressure. This process is controlled by a proportional control logic, which determines the desired mass flow rate of injected water vapour, $\dot{m}^{\mathrm{ref}}_{\mathrm{inj,hc}}$, needed to reach the desired relative humidity setpoint, RH_{set}. Thus, the actual injected flow rate is expressed as:

$$\dot{m}_{\mathrm{inj,hc}} = \dot{m}^{\mathrm{ref}}_{\mathrm{inj,hc}} = k_{\mathrm{p,hc}} (RH_{\mathrm{set}} - RH_{\mathrm{I,hc}}), \tag{43}$$

in which $RH_{\mathrm{I,hc}}$ is the measured relative humidity in the pipe and $k_{\mathrm{p,hc}}$ is the proportional control gain. The energy of water vapour injected is:

$$\Phi_{\mathrm{inj,hc}} = \dot{m}_{\mathrm{inj,hc}} h_{\mathrm{H_2O}}. \tag{44}$$

The specific enthalpy of water, $h_{\mathrm{H_2O}}$, is calculated at the FC stack temperature, as the water generated by the stack is reused. The relative humidity setpoint is treated consistently with the anode side: in the simulations reported in Section 8, it is fixed at 100 % to represent fully humidified reactants at the stack inlet.

3.7. Anode gas channels

The anode gas channels are modelled as a three inlet pipe system. The first inlet receives the gas mixture coming from the humidifier. A portion of this mixture diffuses through the MEA to take part in the electrochemical reactions. Then, the unused gases exit the pipe and recirculate back into the anode network. Both water condensation and heat exchange effects are considered.

The gas mixture dynamics equations are implemented as follows:

$$\frac{dm_{\mathrm{a}}}{dt} = \dot{m}_{\mathrm{out,ha}} - \dot{m}_{\mathrm{H_2,cons}} - \dot{m}_{\mathrm{H_2O,m}} - \dot{m}_{\mathrm{out,a}} - \dot{m}_{\mathrm{cond,a}}, \tag{45a}$$

$$\frac{d\Phi_{\mathrm{a}}}{dt} = \Phi_{\mathrm{out,ha}} - \Phi_{\mathrm{H_2O,m}} - \Phi_{\mathrm{H_2,cons}} - \Phi_{\mathrm{out,a}} - \Phi_{\mathrm{cond,a}} + Q_{\mathrm{cond,a}} + Q_{\mathrm{conv,a}}, \tag{45b}$$

$$\frac{dm_{\mathrm{H_2O,a}}}{dt} = \dot{m}_{\mathrm{H_2O,out,ha}} - \dot{m}_{\mathrm{H_2O,m}} - \dot{m}_{\mathrm{H_2O,out,a}} - \dot{m}_{\mathrm{cond,a}}, \tag{45c}$$

$$\frac{dm_{\mathrm{H_2,a}}}{dt} = \dot{m}_{\mathrm{H_2,out,ha}} - \dot{m}_{\mathrm{H_2,cons}} - \dot{m}_{\mathrm{H_2,out,a}}. \tag{45d}$$

$$\rho_{\mathrm{I,hc}} V_{\mathrm{hc}} \left(\frac{dp_{\mathrm{I,hc}}}{dt} \frac{1}{p_{\mathrm{I,hc}}} - \frac{dT_{\mathrm{I,hc}}}{dt} \frac{1}{T_{\mathrm{I,hc}}} \right) = \frac{dm_{\mathrm{hc}}}{dt} - \frac{R_{\mathrm{N_2}} - R_{\mathrm{H_2O}}}{R_{\mathrm{I}}} \left(\frac{dm_{\mathrm{H_2O,hc}}}{dt} - x_{\mathrm{H_2O}} \frac{dm_{\mathrm{hc}}}{dt} \right) - \frac{R_{\mathrm{N_2}} - R_{\mathrm{O_2}}}{R_{\mathrm{I}}} \left(\frac{dm_{\mathrm{O_2,hc}}}{dt} - x_{\mathrm{O_2}} \frac{dm_{\mathrm{hc}}}{dt} \right), \tag{41a}$$

$$\rho_{\mathrm{I,hc}} c_{\mathrm{v,I}} V_{\mathrm{hc}} \frac{dT_{\mathrm{I,hc}}}{dt} = \frac{d\Phi_{\mathrm{hc}}}{dt} - (u_{\mathrm{H_2O}} - u_{\mathrm{N_2}}) \left(\frac{dm_{\mathrm{H_2O,hc}}}{dt} - x_{\mathrm{H_2O}} \frac{dm_{\mathrm{hc}}}{dt} \right) + (u_{\mathrm{O_2}} - u_{\mathrm{N_2}}) \left(\frac{dm_{\mathrm{O_2,hc}}}{dt} - x_{\mathrm{O_2}} \frac{dm_{\mathrm{hc}}}{dt} \right) - u_{\mathrm{I}} \frac{dm_{\mathrm{hc}}}{dt}. \tag{41b}$$

Box V.

$$\rho_{\mathrm{I,a}} V_{\mathrm{a}} \left(\frac{dp_{\mathrm{I,a}}}{dt} \frac{1}{p_{\mathrm{I,a}}} - \frac{dT_{\mathrm{I,a}}}{dt} \frac{1}{T_{\mathrm{I,a}}} \right) = \frac{dm_{\mathrm{a}}}{dt} - \frac{R_{\mathrm{N_2}} - R_{\mathrm{H_2O}}}{R_{\mathrm{I}}} \left(\frac{dm_{\mathrm{H_2O,a}}}{dt} - x_{\mathrm{H_2O}} \frac{dm_{\mathrm{a}}}{dt} \right) - \frac{R_{\mathrm{N_2}} - R_{\mathrm{H_2}}}{R_{\mathrm{I}}} \left(\frac{dm_{\mathrm{H_2,a}}}{dt} - x_{\mathrm{H_2}} \frac{dm_{\mathrm{a}}}{dt} \right), \tag{51a}$$

$$\rho_{\mathrm{I,a}} c_{\mathrm{v,I}} V_{\mathrm{a}} \frac{dT_{\mathrm{I,a}}}{dt} = \frac{d\Phi_{\mathrm{a}}}{dt} - (u_{\mathrm{H_2O}} - u_{\mathrm{N_2}}) \left(\frac{dm_{\mathrm{H_2O,a}}}{dt} - x_{\mathrm{H_2O}} \frac{dm_{\mathrm{a}}}{dt} \right) + (u_{\mathrm{H_2}} - u_{\mathrm{N_2}}) \left(\frac{dm_{\mathrm{H_2,a}}}{dt} - x_{\mathrm{H_2}} \frac{dm_{\mathrm{a}}}{dt} \right) - u_{\mathrm{I}} \frac{dm_{\mathrm{a}}}{dt}. \tag{51b}$$

Box VI.

In the mass balance Eq. (45a) appears the outlet mass flow rate $\dot{m}_{\mathrm{out,a}}$, that is defined by Eq. (23), and the mass flow rate of hydrogen and water that diffuse into the MEA, respectively $\dot{m}_{\mathrm{H_2,cons}}$ and $\dot{m}_{\mathrm{H_2O,m}}$. $\dot{m}_{\mathrm{H_2,cons}}$ is calculated exploiting the Faraday's law [38], that defines the hydrogen rate consumption, as follows:

$$\dot{m}_{\mathrm{H_2,cons}} = N_{\mathrm{c}} M_{\mathrm{H_2}} \frac{I_{\mathrm{FC}}}{2F}, \tag{46}$$

where $M_{\mathrm{H_2}}$ is the hydrogen molar mass. The energy flow rate associated is evaluated as follows:

$$\Phi_{\mathrm{H_2,cons}} = \dot{m}_{\mathrm{H_2,cons}} h_{\mathrm{H_2}}. \tag{47}$$

The hydrogen specific enthalpy, $h_{\mathrm{H_2}}$, is assessed at the pipe temperature $T_{\mathrm{I,a}}$. While, $\dot{m}_{\mathrm{H_2O,m}}$ is the output of the FC water management model and it is defined by Eq. (89). Thus, $\Phi_{\mathrm{H_2O,m}}$ is defined as:

$$\Phi_{\mathrm{H_2O,m}} = \dot{m}_{\mathrm{H_2O,m}} h_{\mathrm{H_2O}}, \tag{48}$$

where $h_{\mathrm{H_2O}}$ is evaluated either at the pipe temperature or at the FC stack temperature T_{FC} according to the following formulation:

$$h_{\mathrm{H_2O}} = \begin{cases} h_{\mathrm{H_2O}}(T_{\mathrm{I,a}}) & \text{if } \dot{m}_{\mathrm{H_2O,m}} > 0 \\ h_{\mathrm{H_2O}}(T_{\mathrm{FC}}) & \text{if } \dot{m}_{\mathrm{H_2O,m}} < 0 \end{cases}. \tag{49}$$

Moreover, in Eq. (45b) is taken into account the heat exchange through the pipe wall. Both conductive and convective effects are considered, as follows:

$$Q_{\mathrm{cond,a}} = \frac{k_{\mathrm{I}} S_{\mathrm{surf,a}}}{D_{\mathrm{h,a}}} (T_{\mathrm{FC}} - T_{\mathrm{I,a}}), \tag{50a}$$

$$Q_{\mathrm{conv,a}} = \dot{m}_{\mathrm{avg,a}} c_{\mathrm{p,avg}} (T_{\mathrm{FC}} - T_{\mathrm{I,ha}}) \left(1 - \mathrm{e}^{-\frac{h_{\mathrm{a}} S_{\mathrm{surf,a}}}{\dot{m}_{\mathrm{avg,a}} c_{\mathrm{p,avg}}}} \right), \tag{50b}$$

in which is assumed that the pipe wall temperature is equal to the FC stack temperature and that the temperature of the inlet flow rate is equal to the anode humidifier temperature. Then, the dynamics equations of pressure and temperature are reported in Eqs. (51a) and (51b)(see Box VI).

It is worth noting that the volume of the gas channels is calculated by condensing all the channels (squared channels) present in each individual unit cell condensed into a single volume. Therefore, the volume of the FC anode is determined as follows:

$$V_{\mathrm{a}} = S_{\mathrm{a}} l_{\mathrm{a}} = w_{\mathrm{ch,a}}^2 N_{\mathrm{ch,a}} N_{\mathrm{c}} \sqrt{A_{\mathrm{c}}}, \tag{52}$$

where S_{a} is the overall cross-sectional area of the anode gas channels, $w_{\mathrm{ch,a}}$ and l_{a} are the width and length of a single channel, respectively, $N_{\mathrm{ch,a}}$ is the number of channels per unit cell, and A_{c} is the FC unit cell area. Thereby, the surface area is:

$$S_{\mathrm{surf,a}} = 4 \left(\frac{S_{\mathrm{a}}}{D_{\mathrm{h,a}}} \right) l_{\mathrm{a}}, \tag{53}$$

in which $D_{\mathrm{h,a}}$ is the anode gas channels hydraulic diameter.

3.8. Cathode gas channels

The cathode gas channels are modelled following the same approach adopted for the anode channels, accounting for gas exchange with the MEA. The outlet flow rates are regulated by a back-pressure relief valve that is responsible for venting out the unused oxygen and the water produced, as well as for maintaining the correct pressure in the cathode network. The cathode channel equations are the following:

$$\begin{aligned} \frac{dm_{\mathrm{c}}}{dt} =& \dot{m}_{\mathrm{out,hc}} - \dot{m}_{\mathrm{O_2,cons}} + \dot{m}_{\mathrm{H_2O,m}} + \dot{m}_{\mathrm{H_2O,prod}} \\ & - \dot{m}_{\mathrm{out,c}} - \dot{m}_{\mathrm{cond,c}}, \end{aligned} \tag{54a}$$

$$\begin{aligned} \frac{d\Phi_{\mathrm{c}}}{dt} =& \Phi_{\mathrm{out,hc}} - \Phi_{\mathrm{O_2,cons}} + \Phi_{\mathrm{H_2O,m}} + \Phi_{\mathrm{H_2O,prod}} \\ & - \Phi_{\mathrm{out,c}} - \Phi_{\mathrm{cond,c}} + Q_{\mathrm{cond,c}} + Q_{\mathrm{conv,c}}, \end{aligned} \tag{54b}$$

$$\frac{dm_{\mathrm{H_2O,c}}}{dt} = \dot{m}_{\mathrm{H_2O,out,hc}} + \dot{m}_{\mathrm{H_2O}} - \dot{m}_{\mathrm{H_2O,out,c}} - \dot{m}_{\mathrm{cond,c}}, \tag{54c}$$

$$\frac{dm_{\mathrm{O_2,c}}}{dt} = \dot{m}_{\mathrm{O_2,out,hc}} - \dot{m}_{\mathrm{O_2,cons}} - \dot{m}_{\mathrm{O_2,out,c}}. \tag{54d}$$

The term $\dot{m}_{\mathrm{H_2O,m}}$ represents the water exchanged with the MEA, and $\dot{m}_{\mathrm{H_2O,prod}}$ consists in the water produced by the electrochemical reactions, that is evaluated using the Faraday's law [38]:

$$\dot{m}_{\mathrm{H_2O,prod}} = N_{\mathrm{c}} M_{\mathrm{H_2O}} \frac{I_{\mathrm{FC}}}{2F}, \tag{55}$$

where $M_{\mathrm{H_2O}}$ is the water molar mass. $\dot{m}_{\mathrm{H_2O,m}}$ will be defined in Eq. (89), Similarly, the energy fluxes of the water are:

$$\Phi_{\mathrm{H_2O}} = \Phi_{\mathrm{H_2O,prod}} + \Phi_{\mathrm{H_2O,m}}, \tag{56a}$$

$$\Phi_{\mathrm{H_2O,prod}} = \dot{m}_{\mathrm{H_2O,prod}} h_{\mathrm{H_2O}}, \tag{56b}$$

$$\Phi_{\mathrm{H_2O,m}} = \dot{m}_{\mathrm{H_2O,m}} h_{\mathrm{H_2O}}. \tag{56c}$$

In Eq. (56b), $h_{\mathrm{H_2O}}$ is calculated at the FC stack temperature T_{FC}, meanwhile in Eq. (56c) it depends on the flow direction, as follows:

$$h_{\mathrm{H_2O}} = \begin{cases} h_{\mathrm{H_2O}}(T_{\mathrm{FC}}) & \text{if } \dot{m}_{\mathrm{H_2O,m}} > 0 \\ h_{\mathrm{H_2O}}(T_{\mathrm{I,c}}) & \text{if } \dot{m}_{\mathrm{H_2O,m}} < 0 \end{cases}. \tag{57}$$

$$\rho_{\mathrm{I,c}} V_{\mathrm{c}} \left(\frac{dp_{\mathrm{I,c}}}{dt} \frac{1}{p_{\mathrm{I,c}}} - \frac{dT_{\mathrm{I,c}}}{dt} \frac{1}{T_{\mathrm{I,c}}} \right) = \frac{dm_{\mathrm{c}}}{dt} - \frac{R_{\mathrm{N_2}} - R_{\mathrm{H_2O}}}{R_{\mathrm{I}}} \left(\frac{dm_{\mathrm{H_2O,c}}}{dt} - x_{\mathrm{H_2O}} \frac{dm_{\mathrm{c}}}{dt} \right) - \frac{R_{\mathrm{N_2}} - R_{\mathrm{O_2}}}{R_{\mathrm{I}}} \left(\frac{dm_{\mathrm{O_2,c}}}{dt} - x_{\mathrm{O_2}} \frac{dm_{\mathrm{c}}}{dt} \right), \tag{64a}$$

$$\rho_{\mathrm{I,c}} c_{\mathrm{v,I}} V_{\mathrm{c}} \frac{dT_{\mathrm{I,c}}}{dt} = \frac{d\Phi_{\mathrm{c}}}{dt} - (u_{\mathrm{H_2O}} - u_{\mathrm{N_2}}) \left(\frac{dm_{\mathrm{H_2O,c}}}{dt} - x_{\mathrm{H_2O}} \frac{dm_{\mathrm{c}}}{dt} \right) + (u_{\mathrm{O_2}} - u_{\mathrm{N_2}}) \left(\frac{dm_{\mathrm{O_2,c}}}{dt} - x_{\mathrm{O_2}} \frac{dm_{\mathrm{c}}}{dt} \right) - u_{\mathrm{I}} \frac{dm_{\mathrm{c}}}{dt}. \tag{64b}$$

Box VII.

Moreover, $\dot{m}_{\mathrm{O_2,cons}}$ is the oxygen rate of consumption, defined as:

$$\dot{m}_{\mathrm{O_2,cons}} = N_{\mathrm{c}} M_{\mathrm{O_2}} \frac{I_{\mathrm{FC}}}{4F}. \tag{58}$$

The linked energy flow rate $\Phi_{\mathrm{O_2,cons}}$ is:

$$\Phi_{\mathrm{O_2,cons}} = \dot{m}_{\mathrm{O_2,cons}} h_{\mathrm{O_2}}, \tag{59}$$

where $h_{\mathrm{O_2}}$ is evaluated at the pipe temperature. As the cathode gas channels are directly connected to the cathode exhaust, i.e. the relief valve, the outlet flow rate $\dot{m}_{\mathrm{out,c}}$ is defined by the following equation [33]:

$$\dot{m}_{\mathrm{out,c}} = C_{\mathrm{d,c}} S_{\mathrm{v,c}}^{\mathrm{des}} \sqrt{2\rho_{\mathrm{I,c}} |p_{\mathrm{I,c}} - p_{\mathrm{env}}|}. \tag{60}$$

where $C_{\mathrm{d,c}}$ is the pipe discharge coefficient and $S_{\mathrm{v,c}}^{\mathrm{des}}$ is desired the cross-sectional area of the valve. The latter is controlled by a proportional control law that allows to maintain the pressure inside the cathode gas channels close to the reference pressure, as follows:

$$S_{\mathrm{v,c}}^{\mathrm{des}} = k'_{\mathrm{p,c}} (c_{\mathrm{c}} + k_{\mathrm{p,c}} (p_{\mathrm{I,c}} - p_{\mathrm{cathode}}^{\mathrm{ref}})), \tag{61}$$

in which c_{c} is an adding constant, $k_{\mathrm{p,c}}$ and $k'_{\mathrm{p,c}}$ are the proportional control gains, and $p_{\mathrm{cathode}}^{\mathrm{ref}}$ is the anode network reference pressure. The linked outlet energy rate is:

$$\Phi_{\mathrm{out,c}} = \dot{m}_{\mathrm{out,c}} \left(h_{\mathrm{I}} + \frac{1}{2} \left(\frac{\dot{m}_{\mathrm{out,c}}}{\rho_{\mathrm{I,c}} S_{\mathrm{c}}} \right)^2 \right). \tag{62}$$

Furthermore, Eq. (54b) accounts also for the heat exchange through the pipe wall that is composed by both conductive and convective effects, as follows:

$$Q_{\mathrm{cond,c}} = \frac{k_{\mathrm{I}} S_{\mathrm{surf,c}}}{D_{\mathrm{h,c}}} (T_{\mathrm{FC}} - T_{\mathrm{I,c}}), \tag{63a}$$

$$Q_{\mathrm{conv,c}} = \dot{m}_{\mathrm{avg,c}} c_{\mathrm{p,avg}} (T_{\mathrm{FC}} - T_{\mathrm{I,hc}}) \left(1 - \mathrm{e}^{-\frac{h_{\mathrm{c}} S_{\mathrm{surf,c}}}{\dot{m}_{\mathrm{avg,c}} c_{\mathrm{p,avg}}}} \right), \tag{63b}$$

where the pipe wall temperature is assumed equal to the FC stack temperature and that the temperature of the inlet flow rate is equal to the humidifier temperature. Then, the dynamics equations of pressure and temperature are reported in Eq. (64)(see the equations in Box VII). The volume of the cathode channels, V_{c}, and its surface area, $S_{\mathrm{surf,c}}$, are retrieved respectively by means of Eqs. (52) and (53).

3.9. Fuel cell stack

3.9.1. Electrochemistry

The FC is formed by a predefined number of cells, that are stack together to increase the overall output voltage. At each unit cell cathode the electrochemical reaction between hydrogen and oxygen occurs and a voltage is produced, that can be defined by the Nernst's equation [7], as follows:

$$E = E_0 + \frac{RT_{\mathrm{FC}}}{2F} \ln \left(\frac{a_{\mathrm{H_2}} \sqrt{a_{\mathrm{O_2}}}}{a_{\mathrm{H_2O}}} \right), \tag{65}$$

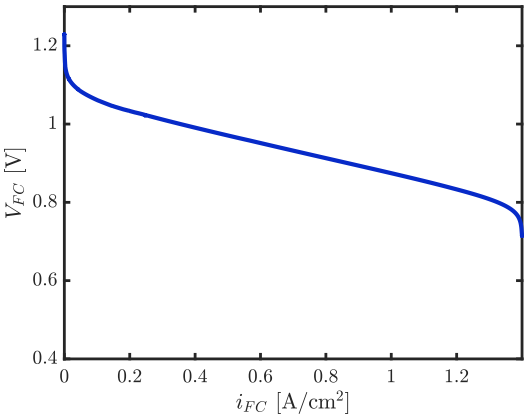

Fig. 3. Polarization curve of the PEMFC stack at nominal operating conditions, computed using the stack dimensioning adopted in the simulations (see Appendix D, Table D.1).

where $E_0 = 1.23$ V is the open circuit voltage, R is the universal gas constant and T_{FC} is the stack temperature. $a_{\mathrm{O_2}}$ and $a_{\mathrm{H_2}}$ are, respectively, the oxygen and hydrogen activities, defined as follows:

$$a_{\mathrm{H_2}} = p_{\mathrm{H_2}} / p_0, \quad a_{\mathrm{O_2}} = p_{\mathrm{O_2}} / p_0, \tag{66}$$

where $p_{\mathrm{H_2}}$ and $p_{\mathrm{O_2}}$ are respectively the hydrogen and oxygen partial pressures inside the MEA and p_0 is a reference pressure, i.e. environment pressure. $p_{\mathrm{H_2}}$ and $p_{\mathrm{O_2}}$ are computed as:

$$p_{\mathrm{H_2}} = \bar{y}_{\mathrm{H_2}} \bar{p}_{\mathrm{an}}, \quad p_{\mathrm{O_2}} = \bar{y}_{\mathrm{O_2}} \bar{p}_{\mathrm{cat}}, \tag{67}$$

in which:

$$\bar{y}_{\mathrm{H_2}} = \frac{y_{\mathrm{H_2,ha}} + y_{\mathrm{H_2,a}}}{2}, \quad \bar{p}_{\mathrm{an}} = \frac{p_{\mathrm{I,ha}} + p_{\mathrm{I,a}}}{2}, \tag{68a}$$

$$\bar{y}_{\mathrm{O_2}} = \frac{y_{\mathrm{O_2,hc}} + y_{\mathrm{O_2,c}}}{2}, \quad \bar{p}_{\mathrm{cat}} = \frac{p_{\mathrm{I,hc}} + p_{\mathrm{I,c}}}{2}, \tag{68b}$$

where $y_{\mathrm{H_2,ha}}$ and $y_{\mathrm{H_2,a}}$ are respectively the hydrogen molar fraction in the anode humidifier and anode gas channels, and $y_{\mathrm{O_2,hc}}$ and $y_{\mathrm{O_2,c}}$ are respectively the oxygen molar fraction in the cathode humidifier and cathode gas channels. Instead, the water activity $a_{\mathrm{H_2O}}$ is evaluated as follows:

$$a_{\mathrm{H_2O}} = p_{\mathrm{H_2O}} / p_{\mathrm{s}}, \tag{69}$$

in which $p_{\mathrm{H_2O}}$ is the partial pressure of the water and p_{s} the water saturation pressure computed at the stack temperature [40]. $p_{\mathrm{H_2O}}$ is evaluated as:

$$p_{\mathrm{H_2O}} = p_{\mathrm{I,c}} y_{\mathrm{H_2O,c}}, \tag{70}$$

where $y_{\mathrm{H_2O,c}}$ is the water molar fraction in the cathode gas channels pipe.

Concerning the fuel cell voltage, different types of losses occur within the stack and contribute to the reduction of the overall output voltage. For clarity, the polarization curve of the simulated PEMFC stack is therefore presented in Fig. 3, computed using the same stack

dimensioning adopted in the simulations (see Appendix D, Table D.1). As commonly observed in PEMFC systems, the polarization curve highlights the progressive voltage drop as the stack current increases, reflecting the combined effects of activation, ohmic, and concentration losses [41]. The losses that are dominant at low current are the activation losses. They are the result of the energy barrier required to overcome the activation of the electrochemical reactions [42]. These losses are described by the Tafel's equation [43]:

$$V_{\text{act}} = \frac{RT_{\text{FC}}}{2\alpha F} \ln\left(\frac{i_{\text{FC}}}{i_0}\right), \tag{71}$$

where i_{FC} is the FC current density, α is the charge transfer coefficient, and i_0 is the exchange current density. The value of i_{FC} can be calculated as:

$$i_{\text{FC}} = \frac{I_{\text{FC}}}{A_{\text{c}}}, \tag{72}$$

where A_{c} is the FC active area. As the Tafel's equation is valid for current densities above the exchange current density i_0, to avoid the non-physical divergence of the Tafel term as $i_{\text{FC}} \rightarrow 0$, we impose $V_{\text{act}} = 0$ whenever the current density is below i_0. The concentration losses, that result from the reduction of reactant concentrations at the electrode sites, are relevant at high current density since the slow dynamics of the gas diffusion through the porous media at the electrode acts as a bottleneck to the reaction [40]. The concentration losses can be calculated as follows [44]:

$$V_{\text{conc}} = \frac{RT_{\text{FC}}}{2F} \ln\left(1 - \frac{i_{\text{FC}}}{i_{\text{L}}}\right), \tag{73}$$

where i_{L} is the maximum limiting current density. Other formulations for concentration losses, including purely exponential or other semi-empirical models, could be adopted within the same framework depending on data availability and modelling objectives. The present parametrization has been selected to provide a good compromise between simplicity and accuracy for the reference PEMFC stack considered. Lastly, the ohmic losses takes into account all the resistance that arise in the MEA.

The ohmic losses can be defined as follows:

$$V_{\text{ohm}} = I_{\text{FC}} R_{\text{m}}, \tag{74}$$

in which R_{m} the resistance of the membrane, defined as the reciprocal of the FC active area times the integral over the membrane thickness t_{m} of the reciprocal of the conductivity [40], as follows:

$$R_{\text{m}} = \frac{1}{A_{\text{c}}} \int_0^{t_{\text{m}}} \frac{dm}{\sigma(\lambda)}, \tag{75}$$

where dm in the infinitesimal membrane thickness. The membrane conductivity σ is a function of the membrane water content λ, which is defined as the ratio of water molecules to the sulphonated sites. The value of σ can be evaluated though an empirical equation [45] as follows:

$$\sigma = \sigma_{30} e^{1268\left(\frac{1}{303.15} - \frac{1}{T_{\text{FC}}}\right)}, \tag{76a}$$

$$\sigma_{30} = \begin{cases} 0.005139\lambda - 0.00326 & \text{if } \lambda > 1 \\ 0.005139 - 0.00326 & \text{if } \lambda < 1 \end{cases}. \tag{76b}$$

The membrane water content λ is calculated as the mean value between the water content at the anode catalyst layer (λ_{acl}) and at the cathode catalyst layer (λ_{ccl}):

$$\lambda = \frac{\lambda_{\text{acl}} + \lambda_{\text{ccl}}}{2} \tag{77}$$

Both λ_{acl} and λ_{ccl} are a function of, respectively, the water activity at the anode ($a_{\text{H}_2\text{O,acl}}$) and cathode ($a_{\text{H}_2\text{O,ccl}}$) catalyst layer. The general formula that relates the water content at the catalyst layer (CL) and the water activity at the anode or cathode CL is defined as [46]:

$$\lambda_{\text{cl}} = \begin{cases} 0.043 + 17.81 a_{\text{H}_2\text{O,cl}} \\ 0.043 + 17.81 a_{\text{H}_2\text{O,cl}} - 39.85 a_{\text{H}_2\text{O,cl}}^2 + 36 a_{\text{H}_2\text{O,cl}}^3 \\ 14.003 + 1.4(a_{\text{H}_2\text{O,cl}} - 1) \end{cases} \tag{78}$$

if $a_{\text{H}_2\text{O,cl}} < 0$
if $0 \le a_{\text{H}_2\text{O,cl}} \le 1.$
if $a_{\text{H}_2\text{O,cl}} > 1$

The water activities at the catalyst layers are calculated considering the molar concentration of water as follows:

$$a_{\text{H}_2\text{O,cl}} = y_{\text{H}_2\text{O,cl}} \frac{p}{p_{\text{s}}}, \tag{79}$$

where p is either $p_{\text{I,a}}$ or $p_{\text{I,c}}$, and $y_{\text{H}_2\text{O,cl}}$ is either the water molar fraction at the anode or cathode catalyst layer. Water molar fractions are derived using Fick's law for diffusion in porous media. Assuming a constant concentration gradient and solving for the water molar fraction, the formulation becomes [47]:

$$y_{\text{H}_2\text{O,cl}} = y_{\text{H}_2\text{O}} - \frac{\dot{m}_{\text{H}_2\text{O,gdl}} t_{\text{gdl}} RT_{\text{FC}}}{p D_{\text{H}_2\text{O,gdl}} M_{\text{H}_2\text{O}}}, \tag{80}$$

where $y_{\text{H}_2\text{O}}$ is the water molar fraction either in the anode or cathode gas channels, t_{gdl} is the thickness of the gas diffusion layer, $D_{\text{H}_2\text{O,gdl}}$ is the water diffusivity at the gas diffusion layer, and $\dot{m}_{\text{H}_2\text{O,gdl}}$ is the water flow rate that diffuses into the gas diffusion layer. Concerning the latter variable, on the anode side it equals to the water flow through the membrane (Eq. (89)), while on the cathode side it is defined as the sum of the water flow through the membrane, $\dot{m}_{\text{H}_2\text{O,m}}$, and the water produced, $\dot{m}_{\text{H}_2\text{O,prod}}$:

$$\dot{m}_{\text{H}_2\text{O,gdl}} = \begin{cases} \dot{m}_{\text{H}_2\text{O,m}} & \text{anode} \\ -(\dot{m}_{\text{H}_2\text{O,m}} + \dot{m}_{\text{H}_2\text{O,prod}}) & \text{cathode} \end{cases}. \tag{81}$$

Then, the output voltage of the FC stack is given by:

$$V_{\text{FC}} = N_{\text{c}}(E - V_{\text{act}} - V_{\text{conc}} - V_{\text{ohm}}). \tag{82}$$

It worth noticing that additional ohmic losses associated with the electrodes, bipolar plates, and interfacial contact resistances may be considered by condensing into an equivalent constant resistance placed after the fuel cell stack.

3.9.2. Water management model

It is well known that evaluating the water content inside the membrane is crucial for a better understanding of the FC behaviour [45]. All the physical phenomena that affect the water transport are considered: the electro-osmotic drag, the back-diffusion transport, and pressure gradient transport [46]. The electro-osmotic drag accounts for the water molecules transported due to hydrogen protons drag, which molar flux is defined as:

$$N_{\text{osm}} = n_{\text{d}} \frac{i_{\text{FC}}}{F}, \tag{83}$$

where n_{d} is the electro-osmotic drag coefficient, defined as follows:

$$n_{\text{d}} = \begin{cases} 0.0029\lambda_{\text{acl}}^2 + 0.05\lambda_{\text{acl}} & \text{if } \lambda_{\text{acl}} \ge 0 \\ 0.05\lambda_{\text{acl}} & \text{if } \lambda_{\text{acl}} < 0 \end{cases}, \tag{84}$$

where λ_{acl} is evaluated by means of Eq. (78). The back-diffusion transport arises from differences in water concentrations at anode and cathode catalyst layers. This gradient is due to differences in humidity in anode and cathode [48]. As a result, a water flux arises to balance the concentrations. It is defined as follows [16]:

$$N_{\text{diff}} = \frac{D_{\text{H}_2\text{O,diff}}}{t_{\text{m}}} \left(C_{\text{H}_2\text{O,acl}} - C_{\text{H}_2\text{O,ccl}}\right), \tag{85}$$

where $D_{\text{H}_2\text{O,diff}}$ is the water back-diffusion coefficient, $C_{\text{H}_2\text{O,acl}}$ and $C_{\text{H}_2\text{O,ccl}}$ are respectively the water concentration at anode and cathode

catalyst layer. The water concentration either at anode or cathode catalyst layer can be defined as follows:

$$C_{H_2O,cl} = \frac{\rho_{m,dry}}{M_{m,dry}} \lambda_{cl}, \tag{86}$$

where $\rho_{m,dry}$ is the dry membrane density and $M_{m,dry}$ is the membrane molar mass. The water content at anode and cathode catalyst layer are calculated with Eq. (78). Whereas, the water back-diffusion coefficient is defined as [46]:

$$D_{H_2O,diff} = 1.25 \cdot 10^{-6} e^{2416\left(\frac{1}{303.15} - \frac{1}{T_{FC}}\right)}. \tag{87}$$

When the pressure of anode and cathode are not equal, a water flow arises due to the pressure gradient. The resultant molar flow rate is defined exploiting the Darcy's law [40]:

$$N_{hydr} = \begin{cases} p_{I,a} K_d \frac{(p_{I,a} - p_{I,c}) y_{H_2O,acl}}{R T_{FC} \mu_{H_2O} t_m} & \text{if } p_{I,a} > p_{I,c} \\ p_{I,c} K_d \frac{(p_{I,a} - p_{I,c}) y_{H_2O,ccl}}{R T_{FC} \mu_{H_2O} t_m} & \text{if } p_{I,a} < p_{I,c} \end{cases} \tag{88}$$

in which K_d is the Darcy's constant, equal to $1{,}58 \cdot 10^{-14}$ cm^2, and μ_{H_2O} is the dynamic viscosity of water calculated at FC stack temperature. Therefore, the overall water flow through the membrane is:

$$\dot{m}_{H_2O,m} = M_{H_2O} A_c N_c (N_{osm} + N_{diff} + N_{hydr}). \tag{89}$$

3.9.3. Fuel cell efficiency

The FC efficiency can be defined as:

$$\eta_{FC} = \frac{P_{el}}{P_{H_2}}, \tag{90}$$

where P_{el} is the electrical power output of the FC and P_{H_2} is the chemical power of the consumed hydrogen. The output power can be defined as follows:

$$P_{el} = V_{FC} I_{FC}. \tag{91}$$

The hydrogen power can be defined exploiting either the Higher Heating Value (HHV) or the Lower Heating Value (LHV). Taking into account the HHV, P_{H_2} is defined as:

$$P_{H_2} = \frac{\dot{m}_{H_2,cons} HHV}{M_{H_2}}. \tag{92}$$

By substituting the definition of $\dot{m}_{H_2,cons}$ (see Eq. (46)), the efficiency becomes:

$$\eta_{FC} = \frac{V_{FC} 2F}{HHV}. \tag{93}$$

In a rigorous sense, Eq. (93) refers to the thermal efficiency of the FC, meaning that this efficiency only accounts for the losses inside the FC. If a broader perspective is to be taken, and thus the overall system efficiency is to be evaluated, the energy consumed by the BoP components must also be considered.

3.9.4. Fuel cell thermodynamics

The FC is characterized by the following power balance [40]:

$$\sum_i (\Phi_i)_{in} = \sum_i (\Phi_i)_{out} + P_{el} + Q_{gen}. \tag{94}$$

As inputs, there are the inlet energy flow rates of the hydrogen, oxygen and water vapour ($\sum_i (\Phi_i)_{in}$), while as output there are the gas energy flow rates exiting the FC ($\sum_i (\Phi_i)_{out}$), the electrical power produced (P_{el}), and the heat generated (Q_{gen}). The difference between the inlet and outlet gas flow rates is essentially the power associated to the reactants and products of the electrochemical reaction, as follows:

$$\sum_i (\Phi_i)_{in} - \sum_i (\Phi_i)_{out} = \Phi_{H_2} + \Phi_{O_2} - \Phi_{H_2O}. \tag{95}$$

where:

$$\Phi_{H_2} = \dot{m}_{H_2,cons} LHV, \tag{96a}$$

$$\Phi_{O_2} = \dot{m}_{O_2,cons} (h_{O_2} - h_{O_2,std}), \tag{96b}$$

$$\Phi_{H_2O} = \dot{m}_{H_2O,prod} (h_{H_2O} - h_{H_2O,std}). \tag{96c}$$

The specific enthalpies h_{O_2} and h_{H_2O} are evaluated at the FC stack temperature, while $h_{O_2,std}$ and $h_{H_2O,std}$ are the specific enthalpies at standard condition. Whereas, for hydrogen is considered the LHV. P_{el} is defined by Eq. (91), thus, from Eq. (94) can be retrieved the heat produced Q_{gen}. Subsequently, the FC stack temperature T_{FC} can be evaluated with the following differential equation:

$$\dot{T}_{FC} = \frac{Q_{gen} - Q_{cc}}{c_{p,m} \rho_m V_m}, \tag{97}$$

in which Q_{cc} is the heat dissipated by the cooling system, $c_{p,m}$, ρ_m and V_m are respectively the overall specific heat, density and volume of the membrane electrode assembly.

3.10. Cooling system

The cooling system is composed by: FC coolant channels, coolant tank, radiator and coolant pump. The pump extracts the appropriate amount of fluid from the coolant tank and puts it into circulation. The heat is extracted by the coolant into the FC coolant channels and then exchanged through the radiator. Water is considered as coolant.

3.10.1. Fuel cell cooling channels

This component is modelled as a two-inlet pipe with the following assumptions: (i) rigid pipe wall, (ii) compressible liquid, (iii) liquid inertia negligible, (iv) viscous friction negligible, (v) gravity effects negligible. As the dynamic compressibility of the coolant is considered, the mass and energy conservation equations in the pipe are [33]:

$$V_{cc} \rho_{I,cc} \left(\frac{1}{\beta} \frac{dp_{I,cc}}{dt} - \alpha_T \frac{dT_{I,cc}}{dt} \right) = \dot{m}_{in,cc} - \dot{m}_{out,cc}, \tag{98a}$$

$$V_{cc} \frac{d(\rho_{I,cc} u_{I,cc})}{dt} = \Phi_{in,cc} - \Phi_{out,cc} + Q_{cc}, \tag{98b}$$

where $p_{I,cc}$, $T_{I,cc}$, $\rho_{I,cc}$ $u_{I,cc}$ are respectively the coolant pressure, temperature, density and internal energy in the channels, V_{cc} is the pipe volume, α_T is the coolant isobaric thermal expansion coefficient, and β is the isothermal bulk modulus. The outlet flow rate $\dot{m}_{out,cc}$ and outlet energy flow rate $\Phi_{out,cc}$ are defined respectively as:

$$\dot{m}_{out,cc} = k_{f,cc} (p_{I,cc} - p_{I,ct}), \tag{99a}$$

$$\Phi_{out,cc} = \dot{m}_{out,cc} h_{I,cc}, \tag{99b}$$

in which $k_{f,cc}$ is the coolant channels outlet flow constant, $h_{I,cc}$ is the coolant channels specific internal energy, and $p_{I,ct}$ is the coolant tank internal pressure. Similarly, the inlet mass and energy flow rates are evaluated as:

$$\dot{m}_{in,cc} = \dot{m}_{out,rad} = k_{f,rad} (p_{I,rad} - p_{I,cc}), \tag{100a}$$

$$\Phi_{in,cc} = \Phi_{out,rad} = \dot{m}_{out,rad} h_{I,rad}, \tag{100b}$$

where $k_{f,rad}$ is the radiator outlet flow constant, $h_{I,rad}$ is the radiator specific internal energy, and $p_{I,rad}$ is the radiator internal pressure. Then, the heat exchanged through the pipe walls, Q_{cc}, is modelled taking into account both conductive and convective contributions, as follows:

$$Q_{cc} = Q_{cd,cc} + Q_{cv,cc}, \tag{101}$$

in which $Q_{cv,cc}$ and $Q_{cd,cc}$ are:

$$Q_{cd,cc} = \frac{k_{l,cc} S_{surf,cc}}{D_{h,cc}} (T_{FC} - T_{l,cc}), \tag{102a}$$

$$Q_{cv,cc} = \dot{m}_{avg,cc} c_{p,avg,cc} (T_{FC} - T_{l,rad}) \left(1 - e^{-\frac{h_{cc} S_{surf,cc}}{\dot{m}_{avg,cc} c_{p,avg,cc}}}\right), \tag{102b}$$

where the pipe wall temperature is equal to FC stack temperature and the temperature of inlet flow is equal to the radiator internal temperature. The total volume is calculated considering that the FC coolant channels consist of a single square channel that passes through the FC multiple times, forming multiple layers. Therefore, it is determined as follows:

$$V_{cc} = S_{cc} l_{cc} = w_{cc}^2 N_{l,cc} N_{p,cc} \sqrt{A_c}, \tag{103}$$

where S_{cc} is the overall cross-sectional area of the coolant channels, w_{cc} and l_{cc} are the width and length of a single channel, $N_{l,cc}$ is the number of layers in stack and $N_{p,cc}$ is the number of passes per layer. Consequently, is also evaluated the surface area $S_{surf,cc}$:

$$S_{surf,cc} = 4 \left(\frac{S_{cc}}{D_{h,cc}}\right) l_{cc}, \tag{104}$$

in which $D_{h,cc}$ is the hydraulic diameter of the coolant channels.

3.10.2. Coolant pump

The coolant pump is modelled as an ideal pump that provides the reference mass flow rate defined by a control algorithm. The work spent by the pump is considered isentropic and it is added to the coolant energy flow [33]:

$$\Phi_{work,p} = \frac{\dot{m}_p^{ref} (p_{l,rad} - p_{l,ct})}{\rho_{avg,p}}, \tag{105}$$

in which ρ_{avg} is the mean density between inlet and outlet:

$$\rho_{avg,p} = \frac{\rho_{l,rad} + \rho_{l,ct}}{2}, \tag{106}$$

where $\rho_{l,rad}$ and $\rho_{l,ct}$ are respectively the coolant density in the radiator and in the coolant tank. While, $\dot{m}_p^{ref}$ is the flow rate imposed by the control algorithm. Indeed, the pump command is created by a proportional-integrative control logic that acts on the tracking error of the FC temperature and a temperature of reference:

$$\dot{m}_p^{ref} = k_{P,p} \left((T_{FC}^{ref} - T_{FC}) + k_{I,p} \int_0^t (T_{FC}^{ref} - T_{FC}) dt\right). \tag{107}$$

$k_{P,p}$ and $k_{I,p}$ are the proportional and integral gain of the proportional-integrative controller and T_{FC}^{ref} is the FC reference temperature.

3.10.3. Coolant tank

The coolant tank is modelled as a variable volume chamber with one outlet. One side is free to move without any load, so internal pressure is constant and equal to the environment pressure. The following assumption are made: (i) liquid compressibility negligible, (ii) rigid chamber, (iii) heat exchange negligible, (iv) resistances negligible.

Thus, the mass conservation is defined as [33]:

$$\dot{m}_{ct} = \rho_{l,ct} S_{ct} v_{ct}, \tag{108}$$

where v_{ct} is the translational velocity of the free-moving side and S_{ct} is the cross-sectional area of the chamber. The sign of v_{ct} sets the flow direction, a positive sign means that the flow enters into the chamber. Specifically, $\dot{m}_{ct}$ is calculated as:

$$\dot{m}_{ct} = \dot{m}_{out,cc} - \dot{m}_p^{ref}. \tag{109}$$

Then, the energy conservation equation is defined as [33]:

$$V_{ct} \frac{d(\rho_{l,ct} u_{l,ct})}{dt} = \Phi_{ct} - p_{l,ct} S_{ct} v_{ct}, \tag{110}$$

in which $u_{l,ch}$ in the coolant internal energy, $V_{l,ch}$ is the tank volume. As the chamber has a free moving side, p_{ch} is equal to p_{env}. The energy flow rate Φ_{ct} is defined according to the flow direction, as follows:

$$\Phi_{ct} = \begin{cases} \dot{m}_{ct} h(P_{l,ct}, T_{l,cc}) & \text{if } \dot{m}_{ct} > 0 \\ \dot{m}_{ct} h(P_{l,ct}, T_{l,ct}) & \text{if } \dot{m}_{ct} < 0 \end{cases}. \tag{111}$$

3.11. Radiator

The radiator is modelled as a two inlet pipe exploiting the same assumption of the FC coolant channels.

Geometrically, it is modelled as a finned tube radiator, while the mass and energy conservation equations are defined as follows:

$$V_{rad} \rho_{l,rad} \left(\frac{1}{\beta} \frac{dp_{l,rad}}{dt} - \alpha_T \frac{dT_{l,rad}}{dt}\right) = \dot{m}_{in,rad} - \dot{m}_{out,rad}, \tag{112a}$$

$$V_{rad} \frac{d(\rho_{l,rad} u_{l,rad})}{dt} = \Phi_{in,rad} - \Phi_{out,rad} + Q_{rad}. \tag{112b}$$

The outlet flow rate $\dot{m}_{out,rad}$ and outlet energy flow rate $\Phi_{out,rad}$ are respectively defined in Eqs. (100a) and (100b). The inlet mass and energy flow rates are evaluated as:

$$\dot{m}_{in,rad} = \dot{m}_p^{ref}, \tag{113a}$$

$$\Phi_{in,rad} = \Phi_{work,p} + \Phi_{out,cc} - \Phi_{cv}. \tag{113b}$$

The total heat exchanged through the pipe walls is evaluated as:

$$Q_{rad} = Q_{cd,rad} + Q_{cv,rad}, \tag{114a}$$

$$Q_{cd,rad} = \frac{k_{l,rad} S_{surf,rad}}{D_{h,rad}} (T_{w,rad} - T_{l,rad}), \tag{114b}$$

$$Q_{cv,rad} = \dot{m}_{avg,rad} c_{p,avg,rad} (T_{w,rad} - T_{l,cc}) \left(1 - e^{-\frac{h_{rad} S_{surf,rad}}{\dot{m}_{avg,rad} c_{p,avg,rad}}}\right), \tag{114c}$$

A portion of this heat is absorbed by the radiator itself, causing its temperature to increase, while the remainder is dissipated into the environment. The heat exchanged with the environment is modelled as convective through the following equation [35]:

$$Q_{env} = k_{rad} A_{rad} (T_{w,rad} - T_{env}) \tag{115}$$

where k_{rad} is the radiator convective heat transfer coefficient, A_{rad} is the radiator active surface area, and $T_{w,rad}$ is the pipe wall temperature, which is calculated as follows:

$$\dot{T}_{w,rad} = \frac{Q_{rad} - Q_{env}}{c_{p,rad} m_{rad}}, \tag{116}$$

where $c_{p,rad}$ and m_{rad} are the specific heat and mass of the radiator.

The numerical values of all PEMFC system parameters used in the simulations (e.g. active area, membrane thickness, compressor map coefficients, coolant flow rates) are reported in Appendix D (Table D.1).

4. Battery

Concerning the Li-ion battery, four types of battery models are reported in literature [49–51]:

- Table-based models: they employ tabulated relations between variables, such as open circuit voltage as function of the state of charge. Their accuracy is limited and strictly related to the battery chosen;

- Electrochemical models: they describe the battery behaviour considering the electrochemical processes. They are accurate but require high computational burden resulting not suitable for real-time applications;
- Equivalent circuit models: they model the electrical behaviour of the battery by means of voltage sources, resistors and capacitors. There exist many different models, which accuracy depends of the level of fidelity adopted;
- Data-driven models: they rely on algorithm of machine learning to model batteries. They can be very accurate, especially in capturing not analytically defined behaviour, while require high computational burden.

As the presented work relies on analytical equations, the equivalent circuit strategy is employed. Moreover, this approach requires few information about the battery chosen, such as discharge characteristic. The battery model encompasses a controlled voltage source with a series resistor. The voltage source represents the open circuit voltage (OCV) as a function of state of charge (SOC), while the resistor models the internal resistance. The model assumption are: (i) constant internal resistance, (ii) same parameters for both charging and discharging, (iii) no Peukert effect, (iv) no thermal effect, (v) no self discharge effect, (vi) no aging effect. The discharge equation is the following [52]:

$$V_{bat} = V_0 - K\frac{Q_{max}}{Q_{max} - it}I^* - K\frac{Q_{max}}{Q_{max} - it}\,it + Ae^{(-B\cdot it)} - R_{int}I_{bat}, \tag{117}$$

and the charge equation is:

$$V_{bat} = V_0 - K\frac{Q_{max}}{it + 0.1Q_{max}}I^* - K\frac{Q_{max}}{Q_{max} - it}it + 0.1Q_{max}I^* + Ae^{(-B\cdot it)} - R_{int}I_{bat}, \tag{118}$$

where, V_{bat} is the battery output voltage, A is the exponential zone amplitude, B is the exponential zone inverse time constant, K is the polarization constant, R_{int} is the internal resistance, Q_{max} is the maximum battery capacity, it is the extracted capacity, I_{batt} is the battery current, and I^* is the filtered battery current. V_0 is a constant voltage defined by the equation:

$$V_{full} = V_0 - R_{int}I_{bat,nom} + A, \tag{119}$$

where $I_{bat,nom}$ is the nominal battery current and V_{full} is the fully charged voltage. Since the open circuit voltage generally varies nonlinearly with the SOC, this effect is taken into account in Eq. (117) through the polarization voltage term $KQ_{max}/(Q_{max} - it)it$. Instead, the polarization resistance effect is represented by the term $KQ_{max}/(Q_{max} - it)I^*$ [53]. The same formulation is extended to the charging phase. The parameters A and B are retrieved as follows [54]:

$$A = V_{full} - V_{exp} \quad B = 3/Q_{exp}, \tag{120}$$

in which V_{exp} and Q_{exp} are respectively the voltage and the capacity corresponding to the end of the exponential zone of the battery characteristics. The value of K is evaluated through the equation [52]:

$$V_{exp} = V_0 - K\frac{Q_{max}}{Q_{max} - Q_{exp}}(Q_{exp} + I_{bat,nom}) - R_{int}I_{bat,nom} + Ae^{-3Q_{exp}/Q_{exp}}, \tag{121}$$

It is worth noting that V_{full}, V_{exp}, Q_{exp} and Q_{max} are retrieved from the battery characteristics at nominal current.

The state of charge of the battery is defined as the ratio of the remaining capacity to the total capacity [55]:

$$SOC = 100\left(1 - \frac{\lambda_d \int I_{bat}\,dt}{Q_{max}}\right), \tag{122}$$

where $\int I_{bat}\,dt$ is the extracted capacity and λ_d is the discharge efficiency, that accounts for the non-ideality of the battery charging/discharging. It is assumed to be equal for both discharge and charge.

All battery parameters, including nominal capacity, open-circuit voltage coefficients and internal resistance values, are listed in Table D.1.

5. Electric motor

The electric motor chosen for the proposed model is a brushed DC motor, due to its simplicity and the easiness in speed and torque control [56].

5.1. Electromechanical model

The electrical circuit equation is [57]:

$$V_a = R_{ar}I_a + L_a\frac{dI_a}{dt} + E_a, \tag{123}$$

where V_a and I_a are respectively the armature voltage and current, R_{ar} and L_a are respectively the armature resistance and inductance and E_a is the back-emf created by the rotor windings. The rotor mechanical dynamics follows:

$$T_e = J_m\frac{d\omega_m}{dt} + B_m\omega_m + T_L, \tag{124}$$

where T_e is the motor torque, J_m is the rotor inertia, ω_m is rotor angular speed, B_m is the viscous friction coefficient, and T_L is the load torque. An important relation that links the electrical and the mechanical domains is the proportionality between the motor torque and current:

$$T_e = k_t I_a, \tag{125}$$

and between the back-emf and the rotational speed:

$$E_a = k_e\omega_m. \tag{126}$$

In particular, the motor constant are supposed equal to each other $k_t = k_e = k_m$ [58]. Given that the powertrain is tested under the load cycle representative of a Venetian lagoon *Vaporetto*, it is assumed that a propeller is mechanically coupled to the motor shaft. Consequently, the load torque T_L is expressed as a quadratic function of the motor angular speed ω_m, according to:

$$T_L = a\,\omega_m^2 + b\,\omega_m, \tag{127}$$

where motor and propeller are assumed to rotate at the same speed. The coefficients a and b are derived from proprietary propeller data supplied by the manufacturer; for confidentiality reasons, their numerical values are not disclosed, although the exact relation has been implemented in the simulations.

5.2. Electric motor control

As the DC motor converts electrical energy into mechanical torque, a torque control is necessary for monitoring the motor behaviour. However, due to high cost of torque sensor, it is always preferable to exploit the direct proportionality to the current (see Eq. (125)) [58]. Similarly, it is crucial to keep a control on the rotational speed of the motor. Consequently, it is chosen a control strategy that exploits two cascade feedback controllers: an outer loop (speed control) that is responsible for maintaining the reference motor speed by defining the reference command for the inner loop (current control), which defines the reference armature voltage to satisfy the torque demand. The control laws of the current and speed are, respectively, the following:

$$I_a^{ref} = \frac{1}{k_m}(K_{pc}(\omega_m^{ref} - \omega_m) + K_{ic}\int_0^t(\omega_m^{ref} - \omega_m)dt), \tag{128a}$$

$$V_a^{ref} = E_a + (K_{ps}(I_a^{ref} - I_a) + K_{is}\int_0^t(I_a^{ref} - I_a)dt). \tag{128b}$$

The term E_a is added as feed-forward action. The reference voltage is then fed to the Buck-Boost converter, that is responsible for maintaining this voltage to the motor terminals. Indeed, the duty cycle of the converter is defined by a control logic that exploits $V_{a,ref}$ as reference (see Section 6.2). Focusing on the current control loop, the zero pole cancellation technique is adopted for tuning the controller gains. The gains are defined as follow [58]:

$$K_{pc} = L_a\omega_{cc}, \quad K_{ic} = R_a\omega_{cc}, \tag{129}$$

where ω_{cc} is the crossover frequency. It must be chosen performing a trade off between stability and response time [59]. The output of the current controller, that is the reference voltage V_a^{ref}, must always be a feasible value, thus, it is inserted a saturation and consequently an anti-windup controller which avoids the integral windup. The gain of the anti-windup controller is selected as $K_{aw,c} = 1/K_{pc}$ [60]. Regarding the speed controller, the same procedure is carried on, and the gain coefficients are defined as follows:

$$K_{ps} = 5J_m, \quad K_{is} = J_m\omega_{cs}, \tag{130}$$

in which ω_{cs} is the crossover frequency of the speed control loop. To prevent the inner control loop from influencing the outer control loop., ω_{cs} is chosen five times smaller than ω_{cc} [58]. Analogously, an anti-windup controller is also implemented in the speed controller, as is imposed a saturation on the armature current. The gain chosen is $K_{aw,s} = 1/K_{ps}$.

E-motor, control and drivetrain parameters are summarized in Table D.1.

6. Power conditioning

A DC bus model is employed to accurately represent the link among the driveline components. A parallel configuration between fuel cell and battery is adopted. A boost converter interfaces the fuel cell stack with the DC bus, while a buck–boost converter connects the DC bus to the electric motor. A non-zero resistance is assumed for the wiring, while inductive effects are considered negligible. Based on these assumptions, the governing electrical equations are formulated.

6.1. Boost converter

The converter exploits a pulse-width modulation technique (PWM) and operates in continuous conduction mode (CCM). These assumptions allows to define the output voltage $V_{out,b}$ and the output current $I_{out,b}$ as function of the duty cycle D_b as follow [61]:

$$V_{out,b} = \frac{V_{in,b}}{(1 - D_b)}, \tag{131}$$

$$I_{out,b} = I_{in,b}(1 - D_b), \tag{132}$$

where $V_{in,b}$ is the input voltage and $I_{in,b}$ is the input current, i.e. the FC voltage V_{FC} and current I_{FC} respectively. The proposed model accounts for the dynamics of the capacitor and the inductor. Thus, the equations considered follows:

$$L_b\dot{I}_{in,b} = -(1 - D_b)V_{out,b} + V_{in,b}, \tag{133a}$$

$$C_b\dot{V}_{out,b} = (1 - D_b)I_{in,b} - I_{out,b}, \tag{133b}$$

where L_b is the input inductance and C_b is the output capacitance. Their values are selected so that the continue conduction mode is ensured and the voltage-current ripples are well adsorbed. Thus, the following expressions are adopted [61]:

$$L_b = \frac{V^n_{out,b}(1 - D^n_b)D^n_b}{\Delta I_{L,b} f_{s,b}}, \quad C_b = \frac{I^n_{out,b} D^n_b}{f_{s,b}\Delta V_{out,b}}, \tag{134}$$

in which $f_{s,b}$ is the switching frequency, $\Delta I_{L,b}$ is the maximum inductor current ripple, $\Delta V_{out,b}$ is the maximum output voltage ripples, $V^n_{out,b}$, $I^n_{out,b}$ and D^n_b are respectively the output voltage, current and duty cycle in nominal condition. A current control provides the correct duty cycle value in order to track the FC reference current I^{ref}_{FC}, defined by the energy management system. A proportional–integral controller is employed, as follows:

$$D_b = K_{P,b}(I^{ref}_{FC} - I_{FC}) + K_{I,b}\int_0^t (I^{ref}_{FC} - I_{FC})dt, \tag{135}$$

in which $I_{FC} = I_{in,b}$, $K_{P,b}$ and $K_{I,b}$ are respectively the proportional and integral control gains.

6.2. Buck-Boost converter

On the motor branch in modelled a Buck-Boost converter, adopting the inverting configuration. The converter is designed to work in CCM and it exploit a PWM technique. The conversion laws are:

$$V_{out,bb} = \frac{D_{bb}}{(1 - D_{bb})}V_{in,bb}, \tag{136}$$

$$I_{out,bb} = \frac{(1 - D_{bb})}{D_{bb}}I_{in,bb}, \tag{137}$$

where D_{bb} is the duty cycle, $V_{in,bb}$ and $I_{in,bb}$ are respectively the input voltage and current, $V_{out,bb}$ and $I_{out,bb}$ are respectively the output voltage and current. The dynamics equations of inductor and capacitor are implemented as follows:

$$L_{bb}\dot{I}_{L,bb} = -(1 - D_{bb})V_{out,bb} + V_{in,bb}D_{bb}, \tag{138a}$$

$$C_{bb}\dot{V}_{out,bb} = (1 - D_{bb})I_{L,bb} - I_{out,bb}, \tag{138b}$$

where L_{bb} is the input inductance, C_{bb} is the output capacitance, and $I_{L,bb}$ is the current flowing through the inductor. The value of the capacitance and the inductance are chosen according to the following equations [61]:

$$L_{bb} = \frac{V^n_{out,bb}(1 - D^n_{bb})}{\Delta I_{L,bb} f_{s,bb}}, \quad C_{bb} = \frac{I^n_{out,bb} D^n_{bb}}{f_{s,bb}\Delta V_{out,bb}}, \tag{139}$$

in which $f_{s,bb}$ is the switching frequency, $\Delta I_{L,bb}$ is the maximum inductor current ripple, $\Delta V_{out,bb}$ is the maximum output voltage ripples, $V^n_{out,bb}$, $I^n_{out,bb}$ and D^n_{bb} are respectively the output voltage, current and duty cycle in nominal condition. To define the duty cycle D_{bb} of the converter it is implemented a voltage control, that ensures the tracking of the reference voltage defined by motor cascade control loop, that is V_a^{ref} (see Eq. (128b)). A proportional-integrative control algorithm is used in the following form:

$$D_{bb} = K_{P,bb}(V_a^{ref} - V_{out,bb}) + K_{I,bb}\int_0^t (V_a^{ref} - V_{out,bb})dt, \tag{140}$$

in which $K_{P,bb}$ is the proportional control gain and $K_{I,bb}$ is the integral control gain.

6.3. Energy management system

The Energy Management System is introduced to provide a realistic supervisory power split for the proposed model. It does not introduce a novel contribution of this work. The EMS acts on top of this unified model by providing the fuel cell reference current (and power) and the corresponding battery contribution required to meet the load demand, based on the battery state of charge. In line with established approaches in the literature [62–64], a rule-based strategy is adopted: the fuel cell is commanded to operate close to a prescribed high-efficiency operating region, $P_{FC,opt}$, while the battery buffers fast transients and compensates the residual power. In the simulations, the same EMS is implemented for both the proposed analytical model and the Simscape benchmark, so that differences in the results reflect the underlying physical modelling rather than the supervisory logic. In Fig. 4 is displayed the logic adopted.

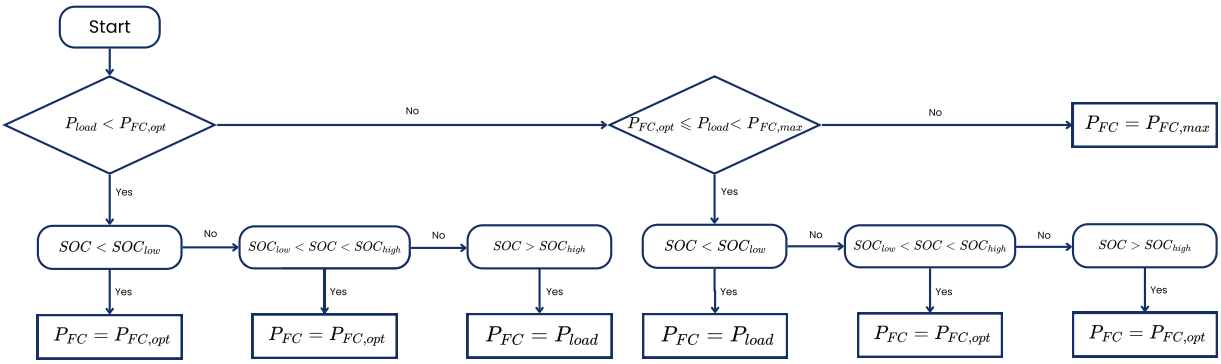

Fig. 4. Block diagram of the rule-based EMS. The supervisory logic sets the fuel cell reference power P_{FC} as a function of load demand and battery SOC, using thresholds SOC_{low} and SOC_{high} and the optimal fuel cell power $P_{FC,opt}$.

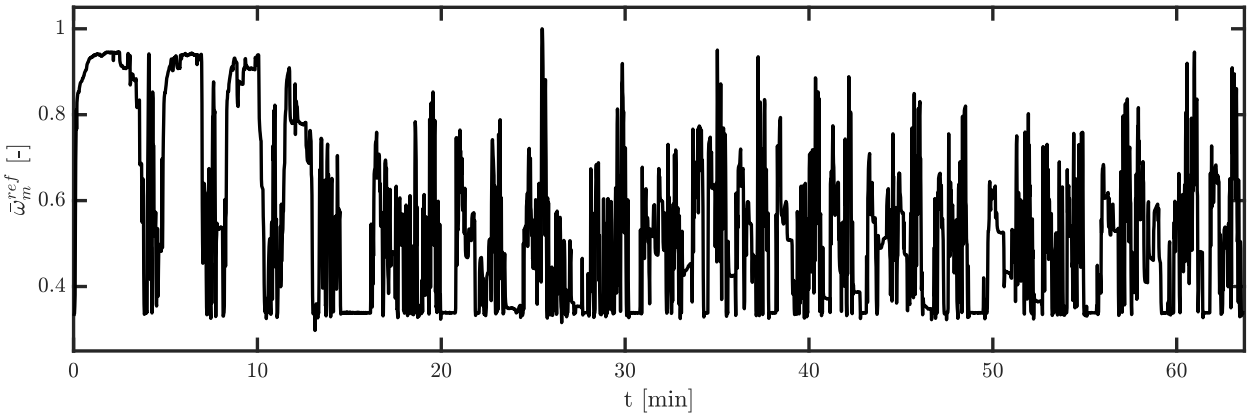

Fig. 5. Normalized load cycle (propeller angular velocity) of the vaporetto on Venice's Line 1. The data were provided by Vulkan Srl and sampled from real operating conditions of the reference waterbus.

7. Simscape model

In order to verify the accuracy and reliability of the proposed analytical model, a benchmark model has been developed using the Simscape environment. The model is designed to be the exact counterpart of the proposed one, using the same component modelling logic and relying on the same assumptions. For the modelling of the various subsystems, predefined Simscape library blocks are employed, as well as custom physics-based representations for specific components, such as the DC Bus. All control laws, including the EMS, are implemented in the Simulink environment. The Simscape components employed, together with the modelling logic adopted for the system construction, are listed in Table C.1, along with the web link to the official documentation. The Simscape implementation leverages the PEM Fuel Cell System model available in the official MathWorks library [65]. This model includes a detailed description of the electrochemistry, thermodynamics, and gas exchange phenomena of a polymer electrolyte membrane fuel cell. Regarding the electrical domain, it is modelled using the Simscape Electrical toolbox. The Boost converter on the FC branch is modelled through the Boost Converter block [66], as well as the Buck-Boost converter [67]. The resistances on the DC bus are evaluated using the Resistor block [68]. The battery is modelled through the Battery block [69] from the Specialized Power Systems library and then linked to the Simscape Electrical domain. The motor is modelled using the DC Motor block [70]. To emulate the mechanical load, an Ideal Torque Source is exploited [71], generating the torque retrieved by the propeller map.

8. Simulations results

As mentioned in the introduction, the normalized load cycle of the Vaporetto operating on Venice's Line 1, provided by Vulkan Srl [28], serves as the basis for this study and was obtained by sampling real operating data. The data, collected over a one-hour period, capture the vessel's typical operational patterns. Fig. 5 illustrates the normalized load cycle used in the analysis. The input to the model is the reference angular velocity at the propeller shaft. The propulsion power demand is derived from the propeller rotational speed profile using standard marine propulsion relations. In particular, the hydrodynamic torque at the propeller shaft is modelled as a quadratic function of the propeller angular speed, as expressed in Eq. (127), and the corresponding mechanical power is obtained as the product of torque and rotational speed. The electric motor and gearbox are modelled as described in Section 5 and the electrical power demand is computed from the mechanical power by accounting for motor and converters efficiencies. As a result, a case study of a propulsion system with a total output power of 130 kW was defined, comprising a 100 kW fuel cell system and a 30 kW battery. All system components are dimensioned accordingly. Table D.1 lists all the parameters used in the simulations.

To ensure clearer visualization of the results, although the simulations were conducted over a time span of approximately 64 min, the temporal evolution of the variables is presented over a 15 min interval. This approach minimizes line overlap and enhances the clarity of the comparison. In all the figures, regardless of the colour, the dashed line represents the output from the proposed *Analytical model*, while the continuous line refers to the *Simscape model* outcome.

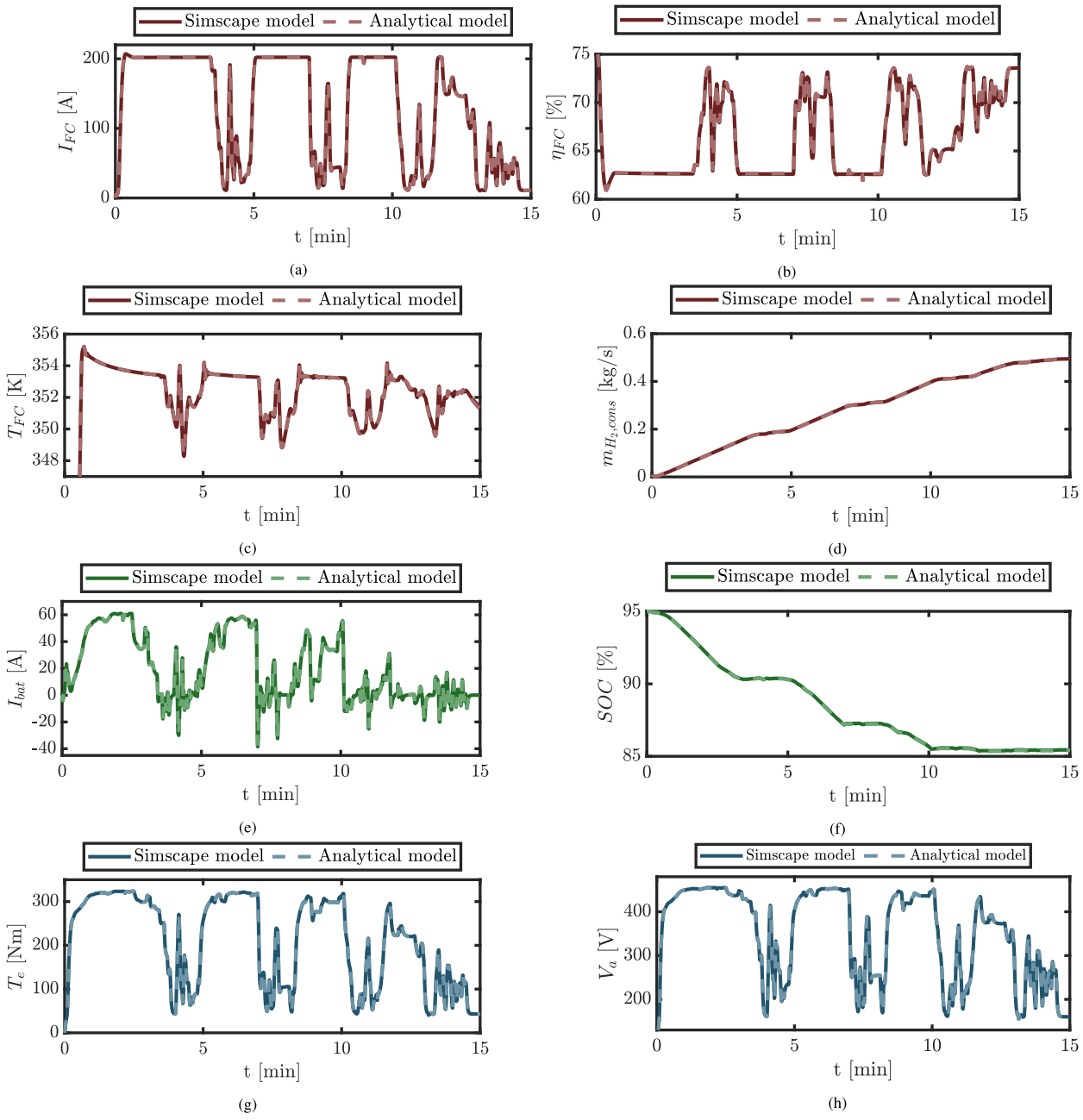

Fig. 6. Graphical comparison between the proposed analytical model and the Simscape benchmark under the same operating conditions. The figure reports: (a) FC current, (b) FC efficiency, (c) FC stack temperature, (d) hydrogen consumed, (e) Battery current and (f) Battery SOC, (g) Motor shaft torque and (h) Motor armature voltage. the time axis is intentionally restricted to a 15 s window to improve readability.

8.1. Accuracy analysis

Firstly, the FC current (Fig. 6(a)), efficiency (Fig. 6(b)), temperature (Fig. 6(c)) and cumulative hydrogen consumption (Fig. 6(d)) obtained with the proposed model are compared against the corresponding results of the Simscape benchmark. The figures show an excellent agreement between the two models in terms of both magnitude and temporal evolution. Only minor discrepancies are observed. In particular, the fuel cell current profiles exhibit nearly identical trends and saturation levels, while the efficiency and temperature trajectories closely match those of the reference model, including the asymptotic stabilization of the stack temperature around the nominal operating value of 80 °C. The cumulative hydrogen consumption further confirms the consistency of the two models over long simulation times.

A similar level of agreement is observed for the battery variables. Figs. 6(e) and 6(f) report the battery current and state of charge, respectively, showing an almost perfect overlap between the analytical model and the Simscape results. The close correspondence of both charging and discharging phases indicates that the proposed model accurately reproduces the power exchange dynamics between the battery and the rest of the powertrain under the same supervisory control logic. Finally, the electric motor variables are compared in Figs. 6(g) and 6(h), which report the motor torque and armature voltage. Also in this case, the two models yield virtually identical results in both amplitude and temporal evolution. The consistency observed across electrical and mechanical quantities confirms that the proposed framework correctly captures the electromechanical coupling of the motor-drive system, matching the behaviour of the high-fidelity Simscape implementation. Once the graphical comparison is conducted, an error analysis is performed on

each relevant variable of the system. The Mean Relative Error (MRE) was used as the error metric, as it provides a straightforward and interpretable measure of model accuracy:

$$\text{MRE} = \frac{1}{N}\sum_{i=1}^{N}\left(\frac{|x_i - y_i|}{y_i}\right)\cdot 100\%, \tag{141}$$

where x_i is the general output variable of the analytical model, y_i is the general output variable of the Simscape model, and N is the number of simulation. Table 8.1 summarizes the MRE values, computed by first averaging the variables over time and subsequently over the 100 simulation runs. For what concerns the FC, the variables that describe its whole behaviour are considered. While, for each BOP component, pressure, temperature, relative humidity and H_2 or O_2 mass fraction are taken into account, this way the internal gas dynamics is perfectly characterized. Regarding the other components of the propulsion, the variables under investigation are essentially electrical, such as voltage, current and power. At the electric motor level, also the mechanical quantities are considered. By observing the table, it is clear that the majority of the MREs stabilize at values below 1 %. This is particularly true when considering the system's electrical variables. The most significant errors arise at the level of the FC balance of plant. Among these, for example, are the mass fractions of hydrogen in the anode network. This can be considered reasonable since the anode network consists of a series of interconnected components with significant complexity, where a single error can propagate in a cascading manner, amplifying subsequent errors. Nevertheless, the average MRE calculated across all the variables is 1.13 %, which means an overall accuracy of 98.87 %. The accuracy increases significantly when an analysis focuses only on the main system variables. For instance, consider the case study where only the following FC variables are taken into account: voltage, current, power, energy, temperature, hydrogen consumption, air compressor power, efficiency, and heat produced, while the variables of the other components remain unchanged. In this scenario, the overall MRE would be 0.17 %, which means an overall accuracy of 99.83 %.

In conclusion, it is important to note that the proposed model does not aim to exceed the benchmark in terms of numerical accuracy, but rather to achieve comparable accuracy while significantly reducing computational complexity. The results presented demonstrate that this objective is met consistently across all tested operating conditions, thereby supporting the suitability of the model for fast system-level simulations and iterative design workflows.

8.2. Computational time analysis

The analysis is performed over 100 simulations for both the analytical and Simscape models. As input of the simulations, it is employed the same load cycle presented in the previous section (Fig. 5). The simulations were run on a personal computer that exploits, as processor, a 13th Gen Intel(R) Core(TM) i7-1355U, 10 core, 1.70 GHz, 5 GHz boost.

Table 8.2 reports the mean simulation times of the two models. The average values were computed by excluding a limited number of outliers, primarily occurring during the initial runs and associated with MATLAB environment initialization and solver setup routines. Under identical hardware and solver settings, the analytical Simulink model achieves a mean simulation time of 3.24 s, compared to 139.5 s for the Simscape benchmark, corresponding to a reduction in computational cost by a factor of approximately 43. Fig. 7 complements this analysis by showing the full distributions of the computational times through boxplots, including outliers. Both models exhibit narrow interquartile ranges, indicating good repeatability. Simscape shows a larger absolute dispersion and a higher number of upper outliers. To enable a fair comparison, the relative variability is quantified through the coefficient of variation, defined as:

$$CV = \frac{\sigma}{\mu}, \tag{142}$$

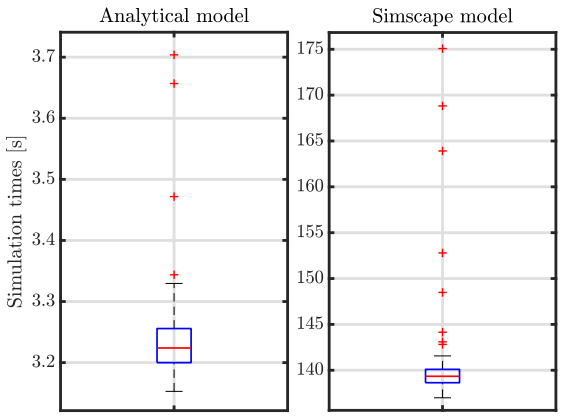

Fig. 7. Boxplots of the computational time distributions for the analytical model and Simscape model obtained over 100 simulations. Different y-axes are used due to the distinct time scales and include outliers to provide a complete statistical characterization.

where σ is the standard deviation and μ the mean value. The coefficients of variation are low for both models, being 2.4 % for the analytical model and 3.9 % for Simscape model, indicating good repeatability in both cases, with a slightly more stable behaviour observed for the Simulink implementation.

8.3. Analysis under transient and abnormal operating conditions

In order to assess the robustness and dynamic capabilities of the proposed model, additional case studies were carried out under both transient and abnormal operating conditions.

8.3.1. Abnormal operating condition

A first study investigates model performance under an abnormal operating condition representative of a balance-of-plant fault. For benchmarking, the same analysis is conducted using the reference Simscape model. Both models are subjected to the duty cycle shown in Fig. 5 until a prescribed time instant, at which the anode and cathode humidifiers are intentionally switched off, preventing humidified air supply. The results are reported in Fig. 8. Focusing on the analytical model (Fig. 8(a)), the humidifier shutdown at $t = 350$ s induces an immediate drop in fuel cell voltage and current, which is compensated by an increased battery current to satisfy the power demand. This behaviour is attributed to an increase in the internal resistance of the polymer electrolyte membrane caused by reduced hydration. Overall, the proposed model captures the system response to humidifier failure as expected, including voltage degradation and the associated water balance dynamics.

Examining the Simscape results reported in Fig. 8(b), a zoomed-in view over a reduced temporal window, approximately 10 s after the humidifier shutdown, is shown to better resolve the transient response. Under these conditions, the Simscape model fails to robustly handle the abnormal scenario: electrical variables exhibit physically inconsistent dynamics, with peak values up to three orders of magnitude larger than those observed under nominal operation. This behaviour is triggered by the collapse of the fuel cell current, which instantaneously shifts the power demand to the battery beyond its admissible limits. The resulting constraint violations propagate through the model, leading to divergent voltage and current trajectories. This response is likely related to the internal logic of the Simscape blocks, where built-in error handling may override a purely physics-based evolution.

Table 8.1
Mean Relative Error (MRE) between the proposed analytical model and the Simscape benchmark for the most relevant system variables, computed over the entire simulation horizon and averaged over 100 simulations.

Component	Variable	Symbol	MRE [%]	Component	Variable	Symbol	MRE [%]
Fuel cell	Voltage	V_{FC}	0.14	Cathode humidifier	Pressure	$p_{I,hc}$	0.07
	Current	I_{FC}	0.33		Temperature	$T_{I,hc}$	0.02
	Reference current	I_{FC}^{ref}	0.31		RH	$RH_{I,hc}$	0.11
	Output power	P_{FC}	0.27		O_2 mass fraction	$x_{O_2,hc}$	0.25
	Energy produced	E_{FC}	0.054	Cathode gas channels	Pressure	$p_{I,c}$	0.07
	Heat produced	Q_{gen}	0.89		Temperature	$T_{I,c}$	0.22
	Temperature	T_{FC}	0.014		RH	$RH_{I,c}$	3.8
	Efficiency	η_{FC}	0.14		O_2 mass fraction	$x_{O_2,c}$	2.88
	H_2 mass consumed	$m_{H_2,cons}$	0.11	Cooling system	FC c.c. temperature	$T_{I,cc}$	0.69
Hydrogen tank	Pressure	$p_{I,t}$	0.014		Radiator temperature	$T_{I,rad}$	1.84
	Temperature	T_t	0.004	Battery	Voltage	V_{bat}	0.16
Anode recirculation	Pressure	$p_{I,r}$	0.18		Current	I_{bat}	0.21
	Temperature	$T_{I,r}$	0.24		State of charge	SOC	0.035
	RH	$RH_{I,r}$	0.92		Output power	P_{bat}	0.16
	H_2 mass fraction	$x_{H_2,r}$	13.3		Energy produced	E_{bat}	0.21
Anode humidifier	Pressure	$p_{I,ha}$	0.15	Electric motor	Voltage	V_a	0.071
	Temperature	$T_{I,ha}$	0.29		Current	I_a	0.14
	RH	$RH_{I,ha}$	0.096		Reference voltage	V_a^{ref}	0.071
	H_2 mass fraction	$x_{H_2,ha}$	11.2		Motor torque	T_e	0.14
Anode gas channels	Pressure	$p_{I,a}$	0.15		Load torque	T_L	0.14
	Temperature	$T_{I,a}$	0.26		Shaft velocity	ω_m	0.07
	RH	$RH_{I,a}$	3.64		Electrical power	$P_{m,el}$	0.2
	H_2 mass fraction	$x_{H_2,a}$	17.18		Mechanical power	$P_{m,mech}$	0.2
Air compressor	Pressure	$p_{I,hc}$	0.07	Boost converter	Output voltage	$V_{out,b}$	0.018
	Temperature	$T_{I,hc}$	0.043		Output current	$I_{out,b}$	0.27
	RH	$_{I,cp}$	0.9	Buck-Boost converter	Output voltage	$V_{out,bb}$	0.018
	O_2 mass fraction	$x_{O_2,cp}$	$4.4 \cdot 10^{-7}$		Output current	$I_{out,bb}$	0.27
	Power	$\Phi_{work,cp}$	0.39				
Overall mean relative error						**1.13%**	

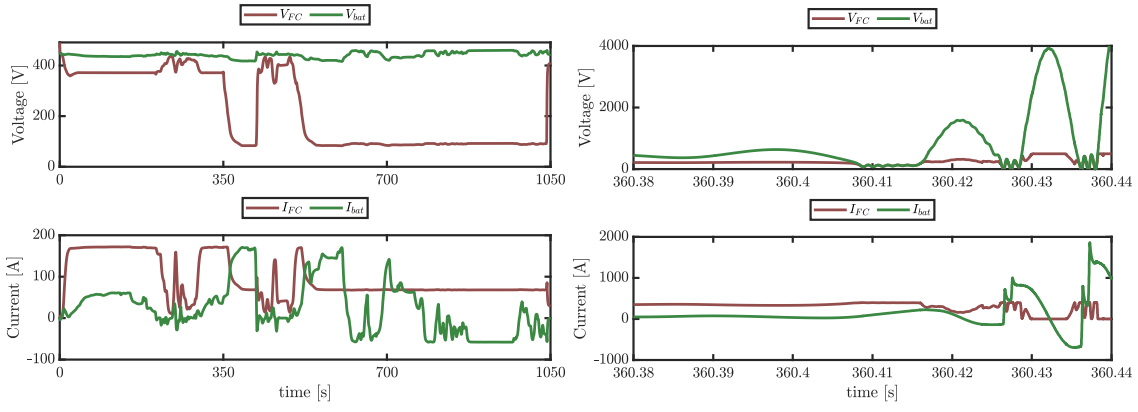

Fig. 8. Comparison between the analytical model and the Simscape benchmark for an abnormal operation condition (FC humidifiers failure at $t = 350$ s): (a) Analytical model results over the full simulation horizon and (b) Simscape model results using a magnified view of the same variable over a restricted time window, focusing on transient events to better illustrate local discrepancies and dynamic response differences.

Table 8.2
Mean simulation time and simulation time ratio.

Mean simulation time [s]		Simulation time ratio [–]
Analytical model	Simscape model	
3.24	139.5	43

8.3.2. *Transient operating condition*

This case study investigates the dynamic response of the proposed model during transient operating conditions. Three scenarios with increasing transient severity are considered, emulating representative operating situations (Fig. 9(a)): a power ramp lasting 5 s, a steeper ramp lasting 1 s, and a quasi-step input. These inputs correspond to different power demands at the motor shaft. Fig. 9(b) reports the temporal evolution of the current required by the motor, together with the contributions provided by the battery and the fuel cell. The results highlight the markedly different dynamic characteristics of the two energy sources. As expected, the fuel cell exhibits a significantly slower response in supplying the requested power, whereas the battery reacts on a much shorter time scale. Consequently, during the initial phase of each transient event, the battery supplies the majority of the current demanded by the load, with this effect becoming more pronounced as the transient steepness increases. In the subsequent phase, the fuel cell current gradually rises and progressively compensates for the battery contribution, eventually becoming the dominant power source. Overall,

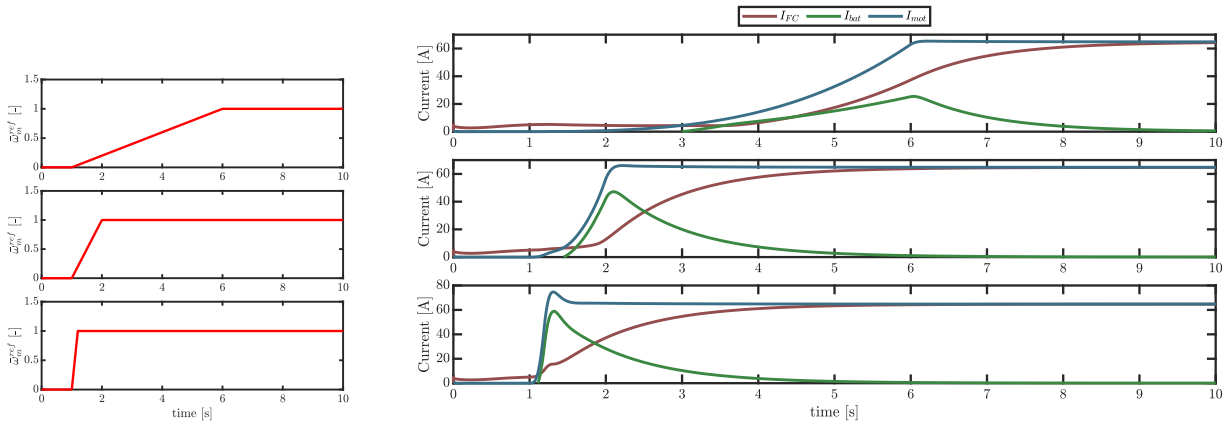

Fig. 9. Transient response of the propulsion system under three scenarios with increasing severity. (a) Normalized motor shaft angular velocity profiles corresponding to three representative operating conditions (from top to bottom): a power ramp lasting 5 s, a steeper ramp lasting 1 s, and a quasi-step input. (b) Corresponding fuel cell, battery, and motor currents, highlighting the different dynamic contributions of each subsystem as the transient rapidity increases.

these results provide a qualitative verification that the proposed model captures the expected transient behaviour and the complementary roles of the fuel cell and the battery during fast load variations.

9. Conclusions

The analytical model presented in this study is characterized by multiple physical domains couplings through explicit analytical expressions, enabling accurate and reliable simulations while maintaining a low computational burden. When benchmarked against a detailed Simscape implementation, the proposed model attains an overall accuracy of about 98.87 % across all state variables while reducing the average computation time by roughly one order of magnitude. This combination of accuracy and computational efficiency makes the framework particularly attractive for iterative design studies and for real-time–oriented applications. Moreover, two dedicated case studies have been carried out to assess the reliability of the model in capturing the system's response under particular conditions. In future work, predictive algorithms will be integrated into the framework to evaluate the medium and long-term behaviour of the powertrain, accounting for component aging and lifetime. Beyond the purely simulation-based assessment, experimental campaigns are planned on a down-scaled propulsion system fully analogous to the one modelled, which will provide an experimental validation. Furthermore, the model will be translated into Python in order to make it fully open-source and independent of commercial software such as MATLAB, thereby fostering accessibility and community-driven development.

CRediT authorship contribution statement

Alessandro Brusasco: Writing – review & editing, Writing – original draft, Visualization, Validation, Software, Methodology, Investigation, Formal analysis, Data curation, Conceptualization. **Mauro Bonfanti:** Writing – review & editing, Visualization, Supervision, Project administration, Methodology, Funding acquisition, Formal analysis, Data curation, Conceptualization. **Francesco Balestrieri:** Writing – review & editing, Visualization, Conceptualization. **Giulio Gennaro:** Supervision, Resources, Conceptualization. **Matteo Melchiorre:** Writing – review & editing, Supervision, Methodology. **Stefano Mauro:** Writing – review & editing, Supervision, Funding acquisition.

Declaration of Generative AI and AI-assisted technologies in the writing process

During the preparation of this work, the authors used the AI-based language model ChatGPT by OpenAI, in order to improve the spelling, language, and grammar of this paper. After using these tools/services, the authors reviewed and edited the content as needed and take full responsibility for the content of the publication.

Declaration of competing interest

The authors declare that they have no known competing financial interests or personal relationships that could have appeared to influence the work reported in this paper.

Acknowledgements

This publication is founded by PNRR-NGEU which has received funding from the MUR – DM 630/2024.

This publication is founded by PNRR-NGEU which has received funding from the MUR – DM 117/2023.

This publication is funded by the European Union - NextGenerationEU, Mission 4 Component 2 - ECS000036 - CUP E13B22000020001 with the support of project NAVIGATE, Proof of Concept.

This publication is founded by NODES - North-West Digital and Sustainable- under investment 1.5 "Creation and strengthening of Ecosystems of innovation" and the development of "Territorial R&D leaders" - Call for Academic PoCs under CUP E13B22000020001 funds - Spoke 1.

Appendix A. Parameters nomenclature

See Table A.1.

Appendix B. FC components

See Fig. B.1.

Table A.1
Model parameters nomenclature.

Nomenclature			
m	Gas mixture mass	T_{in}	Inlet mixture temperature
$\dot{m}_{in}$	Gas mixture inlet mass flow rate	h	Heat transfer coefficient
$\dot{m}_{out}$	Gas mixture outlet mass flow rate	N_u	Nusselt number
$\dot{m}_{cond}$	Water vapour rate of condensation	x_{ws}	Specific humidity at saturation
Φ	Gas mixture internal energy	p_{ws}	H_2O saturation pressure
Φ_{in}	Gas mixture inlet rate of energy	τ_{cond}	Condensation time constant
Φ_{out}	Gas mixture outlet rate of energy	ϕ_{ws}	Relative humidity at saturation
Φ_{cond}	H_2O condensation energy rate.	Δh_{vap}	H_2O enthalpy of vaporization
Q	Heat flow rate exchanged through the pipe walls	S_{surf}	Pipe surface area
$\dot{m}_w$	H_2O mass	$\dot{m}_{avg}$	Average mixture mass flow rate
$\dot{m}_{w,in}$	H_2O inlet mass flow rate	$c_{p,avg}$	Average mixture specific heat
$\dot{m}_{w,out}$	H_2O outlet mass flow rate	k_{avg}	Average mixture thermal conductivity
$\dot{m}_g$	Trace gas mass	m_t	Tank hydrogen mass
$\dot{m}_{g,in}$	Trace gas inlet mass flow rate	Φ_t	Tank hydrogen energy
$\dot{m}_{g,out}$	Trace gas outlet mass flow rate	$\dot{m}_{out,t}$	Tank outlet flow rate
k_f	Nozzle constant	$\Phi_{out,t}$	Tank outlet energy flow rate
p_I	Pipe internal pressure	V_t	Tank volume
h_I	Mixture specific enthalpy	$p_{I,t}$	Tank pressure
ρ_I	Mixture internal energy	$T_{I,t}$	Tank temperature
T_I	Mixture temperature	$\rho_{I,t}$	Tank gas mixture density
R_I	Mixture specific gas constant	S_{vt}^{des}	Tank valve desired cross-sectional area
$c_{v,I}$	Mixture specific heat at constant volume	$k_{p,vt}$	Tank valve proportional gain
u_I	Mixture specific internal energy	$k'_{v,t}$	Tank valve modulating coefficient
$h_{T,in}$	Inlet total enthalpy	$C_{d,t}$	Tank valve discharge coefficient
$h_{T,out}$	Outlet total enthalpy	p_{anode}^{ref}	Anode network reference pressure
p_{out}	Pipe outlet pressure	m_r	Recirculation gas mixture mass
V_p	Pipe internal volume	Φ_r	Recirculation gas mixture energy
S_p	Pipe cross-sectional area	$\dot{m}_{out,r}$	Recirculation outlet mass flow rate
h_a	Dry air specific enthalpy	$\Phi_{out,r}$	Recirculation outlet energy flow rate
h_g	Trace gas specific enthalpy	$\dot{m}_{cond,r}$	Recirculation condensation flow rate
h_w	H_2O specific enthalpy	$\Phi_{cond,r}$	Recirculation condensation energy flow rate
x_a	Dry air mass fraction	$m_{H_2O,r}$	Recirculation H_2O mass
x_g	Trace gas mass fraction	$m_{H_2,r}$	Recirculation H_2 mass
x_w	H_2O mass fraction	$\dot{m}_{H_2O,out,r}$	Recirculation outlet H_2O flow rate
u_a	Dry air specific internal energy	$\dot{m}_{H_2,out,r}$	Recirculation outlet H_2 flow rate
u_g	Trace gas specific internal energy	V_r	Recirculation volume
u_w	H_2O specific internal energy	S_r	Recirculation outlet cross-sectional area
R_a	Dry air specific gas constant	$p_{I,r}$	Recirculation pressure
R_g	Trace gas specific gas constant	$T_{I,r}$	Recirculation temperature
R_w	H_2O specific gas constant	$\rho_{I,r}$	Recirculation gas mixture density
$c_{v,a}$	Dry air specific heat at constant volume	$k_{f,r}$	Recirculation outlet flow gain
$c_{v,g}$	Trace gas specific heat at constant volume	$k_{p,r}$	Recirculation blower proportional control gain
$c_{v,w}$	H_2O specific heat at constant volume	$k'_{p,r}$	Recirculation blower proportional control gain
Q_{cond}	Conductive heat flow rate	c_r	Recirculation blower control constant
Q_{conv}	Convective heat flow rate	m_{ha}	Anode humidifier gas mixture mass
k_I	Mixture thermal conductivity	Φ_{ha}	Anode humidifier gas mixture energy
T_w	Pipe walls temperature	$\dot{m}_{out,ha}$	Anode humidifier outlet flow rate
D_h	Hydraulic diameter of the pipe	$\Phi_{out,ha}$	Anode humidifier outlet energy flow rate
$\dot{m}_{cond,ha}$	Anode humidifier condensation flow rate	λ_{O_2}	Oxygen Excess Ratio (OER)
$\Phi_{cond,ha}$	Anode humidifier condensation energy flow rate	$\omega_{cp,max}$	Compressor maximum rotational velocity
$m_{H_2O,ha}$	Anode humidifier H_2O mass	$k_{p,cp}$	Compressor proportional control gain
$m_{H_2,ha}$	Anode humidifier H_2 mass	$k_{I,cp}$	Compressor integral control gain
$\dot{m}_{H_2O,out,ha}$	Anode humidifier outlet H_2O flow rate	$\Phi_{work,cp}$	Compressor power
$\dot{m}_{H_2,out,ha}$	Anode humidifier outlet H_2 flow rate	$S_{cp,in}$	Compressor inlet cross-sectional area
$\dot{m}_{inj,ha}$	Anode humidifier injected H_2O flow rate	m_{hc}	Cathode humidifier gas mixture mass
$\Phi_{inj,ha}$	Anode humidifier injected H_2O energy flow rate	Φ_{hc}	Cathode humidifier gas mixture energy
V_{ha}	Anode humidifier volume	$\dot{m}_{out,hc}$	Cathode humidifier outlet flow rate
S_{ha}	Anode humidifier outlet cross-sectional area	$\Phi_{out,hc}$	Cathode humidifier outlet energy flow rate
$p_{I,ha}$	Anode humidifier pressure	$\dot{m}_{cond,hc}$	Cathode humidifier condensation flow rate
$T_{I,ha}$	Anode humidifier temperature	$\Phi_{cond,hc}$	Cathode humidifier condensation energy flow rate
$\rho_{I,ha}$	Anode humidifier gas mixture density	$m_{H_2O,hc}$	Cathode humidifier H_2O mass
$k_{f,ha}$	Anode humidifier outlet flow gain	$m_{H_2,hc}$	Cathode humidifier H_2 mass
RH_{set}	Relative humidity setpoint	$\dot{m}_{H_2O,out,hc}$	Cathode humidifier outlet H_2O flow rate
$k_{p,ha}$	Anode humidifier proportional control gain	$\dot{m}_{H_2,out,hc}$	Cathode humidifier outlet H_2 flow rate
m_{cp}	Compressor gas mixture mass	$\dot{m}_{inj,hc}$	Cathode humidifier injected H_2O flow rate
Φ_{cp}	Compressor gas mixture energy	$\Phi_{inj,hc}$	Cathode humidifier injected H_2O energy flow rate
$\dot{m}_{in,cp}$	Compressor inlet mass flow rate	V_{hc}	Cathode humidifier volume
$\dot{m}_{out,c}$	Compressor outlet mass flow rate	S_{hc}	Cathode humidifier outlet cross-sectional area
$\Phi_{in,cp}$	Compressor inlet energy flow rate	$p_{I,hc}$	Cathode humidifier pressure
$\Phi_{out,cp}$	Compressor outlet energy flow rate	$T_{I,hc}$	Cathode humidifier temperature
$m_{H_2O,cp}$	Compressor H_2O mass	$\rho_{I,hc}$	Cathode humidifier gas mixture density
$m_{O_2,cp}$	Compressor O_2 mass	$k_{f,hc}$	Cathode humidifier outlet flow gain
$\dot{m}_{H_2O,in,cp}$	Compressor inlet H_2O flow rate	$k_{p,hc}$	Cathode humidifier proportional control gain

(*continued on next page*)

Table A.1 (*continued*).

$\dot{m}_{H_2O,out,cp}$	Compressor outlet H_2O flow rate
$\dot{m}_{O_2,in,cp}$	Compressor inlet O_2 flow rate
$\dot{m}_{O_2,out,cp}$	Compressor outlet O_2 flow rate
V_{cp}	Compressor volume
S_{cp}	Compressor cross-sectional area
$p_{l,cp}$	Compressor pressure
$T_{l,cp}$	Compressor temperature
$\rho_{l,cp}$	Compressor gas mixture density
$k_{f,cp}$	Compressor outlet flow gain
$\dot{m}_{corr}$	Compressor corrected mass flow rate
$p_{in,cp}$	Compressor inlet pressure
$T_{in,cp}$	Compressor inlet temperature
P_{env}	Environmental pressure
T_{env}	Environmental temperature
ρ_{env}	Environmental air density
$x_{O_2,env}$	Environmental O_2 mass fraction
P_{ratio}	Inlet-outlet pressure ratio
ω_{cp}^{ref}	Compressor reference rotational speed
$\dot{m}_{in,cp}^{ref}$	Compressor reference air flow rate
$k_{l,c}$	Cathode gas channels heat transfer coefficient
l_c	Cathode gas channels length
$w_{ch,c}$	Cathode gas channels unit cell width
$N_{ch,c}$	Cathode gas channels number of unit cell
$c_{p,avg,c}$	Cathode gas channels average coolant specific heat
$k_{l,c}$	Cathode gas channels coolant thermal conductivity
$\dot{m}_c$	Cathode gas channels gas mixture mass
Φ_c	Cathode gas channels gas mixture energy
$\dot{m}_{out,c}$	Cathode gas channels outlet flow rate
$\Phi_{out,c}$	Cathode gas channels outlet energy flow rate
$\dot{m}_{cond,c}$	Cathode gas channels condensation flow rate
$\Phi_{cond,c}$	Cathode gas channels condensation energy flow
$m_{H_2O,c}$	Cathode gas channels H_2O mass
$m_{O_2,c}$	Cathode gas channels H_2 mass
$\dot{m}_{H_2O,out,c}$	Cathode gas channels outlet H_2O flow rate
$\dot{m}_{O_2,out,c}$	Cathode gas channels outlet H_2 flow rate
$\dot{m}_{H_2O}$	Cathode gas channels total H_2O flow rate
Φ_{H_2O}	Cathode gas channels total H_2O energy flow rate
V_c	Cathode gas channels volume
S_c	Cathode gas channels cross-sectional area
$S_{surf,c}$	Cathode gas channels surface area
$p_{l,c}$	Cathode gas channels pressure
$T_{l,c}$	Cathode gas channels temperature
$\rho_{l,c}$	Cathode gas channels gas mixture density
$D_{h,c}$	Cathode gas channels hydraulic diameter
$\dot{m}_{avg,c}$	Cathode gas channels average mass flow rate
h_c	Cathode gas channels heat transfer coefficient
$C_{d,c}$	Cathode exhaust valve discharge coefficient
$S_{v,c}^{des}$	Cathode exhaust valve desired cross-sectional area
$k_{p,c}$	Cathode exhaust valve control proportional gain
$k'_{p,c}$	Cathode exhaust valve control proportional gain
c_c	Cathode exhaust valve control adding constant
$P_{cathode}^{ref}$	Cathode network reference pressure
$\dot{m}_{H_2,cons}$	H_2 consumption rate
$\dot{m}_{O_2,cons}$	O_2 consumption rate
$\dot{m}_{H_2O,prod}$	H_2O production rate
$\dot{m}_{H_2O,m}$	H_2O exchanged with MEA
$\Phi_{H_2,cons}$	H_2 consumed energy flow rate
$\Phi_{O_2,cons}$	O_2 consumed energy flow rate
$\Phi_{H_2O,prod}$	H_2O produced energy flow rate
$\Phi_{H_2O,m}$	H_2O energy exchanged with MEA
R_{H_2}	H_2 specific gas constant
R_{O_2}	O_2 specific gas constant
R_{H_2O}	H_2O specific gas constant
h_{H_2}	H_2 specific enthalpy
h_{O_2}	O_2 specific enthalpy
h_{H_2O}	H_2O specific enthalpy
u_{H_2}	H_2 specific internal energy
u_{O_2}	O_2 specific internal energy
u_{H_2O}	H_2O specific internal energy
M_{H_2}	H_2 molar mass
M_{O_2}	O_2 molar mass
N_{hydr}	Pressure gradient molar flux
η_{FC}	FC efficiency
P_{el}	FC output power
P_{H_2}	H_2 chemical power
$\dot{m}_a$	Anode gas channels gas mixture mass
Φ_a	Anode gas channels gas mixture energy
$\dot{m}_{out,a}$	Anode gas channels outlet flow rate
$\Phi_{out,a}$	Anode gas channels outlet energy flow rate
$\dot{m}_{cond,a}$	Anode gas channels condensation flow rate
$\Phi_{cond,a}$	Anode gas channels condensation energy flow rate
$m_{H_2O,a}$	Anode gas channels H_2O mass
$m_{H_2,a}$	Anode gas channels H_2 mass
$\dot{m}_{H_2O,out,a}$	Anode gas channels outlet H_2O flow rate
$\dot{m}_{H_2,out,a}$	Anode gas channels outlet H_2 flow rate
V_a	Anode gas channels volume
S_a	Anode gas channels cross-sectional area
$S_{surf,a}$	Anode gas channels surface area
$p_{l,a}$	Anode gas channels pressure
$T_{l,a}$	Anode gas channels temperature
$\rho_{l,a}$	Anode gas channels gas mixture density
$D_{h,a}$	Anode gas channels hydraulic diameter
$\dot{m}_{avg,a}$	Anode gas channels average mass flow rate
h_a	Anode gas channels heat transfer coefficient
$k_{l,c}$	Anode gas channels heat transfer coefficient
l_a	Anode gas channels length
$w_{ch,a}$	Anode gas channels unit cell width
$N_{ch,a}$	Anode gas channels number of unit cell
$c_{p,avg,a}$	Anode gas channels average coolant specific heat
$k_{l,a}$	Anode gas channels coolant thermal conductivity
M_{H_2O}	H_2O molar mass
E	Nernst's potential
E_0	FC open circuit voltage
R	Universal gas constant
T_{FC}	FC stack temperature
F	Faraday's constant
a_{H_2}	H_2 activity
a_{O_2}	O_2 activity
a_{H_2O}	H_2O activity
p_{H_2}	H_2 partial pressure
p_{O_2}	O_2 partial pressure
p_{H_2O}	H_2O partial pressure
p_0	Reference pressure
i_{FC}	FC current density
I_{FC}	FC current
α	FC charge transfer coefficient
i_0	FC exchange current density
i_L	FC limiting current density
R_m	Membrane resistance
N_c	FC number of cell
A_c	FC active area
σ	Membrane conductivity
λ	Membrane H_2O content
λ_{acl}	Anode CL H_2O content
λ_{ccl}	Cathode CL H_2O content
$a_{H_2O,acl}$	Anode CL H_2O activity
$a_{H_2O,ccl}$	Cathode CL H_2O activity
$y_{H_2O,cl}$	CL H_2O molar fraction
y_{H_2O}	Electrode H_2O molar fraction
t_{gdl}	GDL thickness
$D_{h_2o,gdl}$	GDL H_2O diffusivity
$\dot{m}_{H_2O,gdl}$	GDL H_2O flow rate
V_{act}	Activation losses
V_{conc}	Concentration losses
V_{ohm}	Ohmic losses
V_{FC}	FC output voltage
n_d	FC electro-osmotic drag coefficient
$D_{H_2O,diff}$	H_2O back-diffusion coefficient
$C_{H_2O,acl}$	Anode CL H_2O concentration
$C_{H_2O,ccl}$	Cathode CL H_2O concentration
$\rho_{m,dry}$	Dry membrane density
$M_{m,dry}$	Dry membrane molar mass
K_d	Darcy's constant
μ_{H_2O}	H_2O dynamic viscosity
N_{osm}	Electro-osmotic drag molar flux
N_{diff}	Back-diffusion molar flux
$p_{l,ct}$	Coolant tank pressure
$T_{l,ct}$	Coolant tank temperature
$\rho_{l,ct}$	Coolant tank coolant density
V_{ct}	Coolant tank volume

(*continued on next page*)

Table A.1 (*continued*).

HHV	H_2 Higher Heating Value	S_{ct}	Coolant tank cross-sectional area
LHV	H_2 Lower Heating Value	v_{ct}	Free-moving side translational velocity
Φ_{H_2}	H_2 consumed net energy	$\dot{m}_{in,rad}$	Radiator inlet flow rate
Φ_{O_2}	O_2 consumed net energy	$\dot{m}_{out,rad}$	Radiator outlet flow rate
Φ_{H_2O}	H_2O produced net energy	Q_{rad}	Radiator heat flow rate
$h_{H_2,std}$	H_2 specific enthalpy in standard conditions	$\Phi_{in,rad}$	Radiator inlet energy flow rate
$h_{O_2,std}$	O_2 specific enthalpy in standard conditions	$\Phi_{out,rad}$	Radiator outlet energy flow rate
$h_{H_2O,std}$	H_2O specific enthalpy in standard conditions	Q_{env}	Radiator convective heat flow rate
$c_{p,m}$	Membrane specific heat	V_{rad}	Radiator volume
V_m	Membrane volume	A_{rad}	Radiator active surface area
Q_{gen}	FC heat produced	$p_{l,rad}$	Radiator pressure
Q_a	Anode gas channels heat flow rate	$T_{l,rad}$	Radiator temperature
$Q_{cond,a}$	Anode gas channels conductive heat flow rate	$\rho_{l,rad}$	Radiator coolant density
$Q_{conv,a}$	Anode gas channels convective heat flow rate	k_{rad}	Radiator convective heat transfer coefficient
Q_c	Cathode gas channels heat flow rate	$k_{f,rad}$	Radiator outlet flow constant
$Q_{cond,c}$	Cathode gas channels conductive heat flow rate	$T_{w,rad}$	Radiator wall temperature
$Q_{conv,c}$	Cathode gas channels convective heat flow rate	m_{rad}	Radiator mass
$c_{p,avg,cc}$	Cathode gas channels average coolant specific heat	$S_{surf,rad}$	Radiator surface area
$k_{l,cc}$	FC coolant channels coolant thermal conductivity	$D_{h,rad}$	Radiator hydraulic diameter
$k_{f,cc}$	FC coolant channels outlet flow constant	$c_{p,avg,rad}$	Radiator average coolant specific heat
$N_{l,cc}$	FC coolant channels number of unit cell	$k_{l,rad}$	Radiator coolant thermal conductivity
l_{cc}	FC coolant channels length	$c_{p,rad}$	Radiator specific heat
w_{cc}	FC coolant channels unit cell width	$\dot{m}_{avg,rad}$	Radiator average mass flow rate
$N_{p,cc}$	FC coolant channels number of unit cell	h_{rad}	Radiator heat transfer coefficient
$\dot{m}_{in,cc}$	FC coolant channels inlet flow rate	V_{bat}	Battery output voltage
$\dot{m}_{out,cc}$	FC coolant channels outlet flow rate	I_{bat}	Battery current
$\Phi_{in,cc}$	FC coolant channels inlet energy flow rate	Q_{max}	Battery maximum capacity
$\Phi_{out,cc}$	FC coolant channels outlet energy flow rate	I^*	Battery filtered current
Q_{cc}	FC coolant channels heat flow rate	it	Battery extracted capacity
$Q_{cv,cc}$	FC coolant channels convective heat flow rate	R_{int}	Battery internal resistance
$Q_{cd,cc}$	FC coolant channels conductive heat flow rate	V_0	Battery constant voltage
V_{cc}	FC coolant channels volume	Q_{nom}	Battery nominal capacity
$S_{surf,cc}$	FC coolant channels surface area	Q_{exp}	Battery exponential capacity
$p_{l,cc}$	FC coolant channels pressure	$I_{bat,nom}$	Battery nominal current
$T_{l,cc}$	FC coolant channels temperature	V_{nom}	Battery nominal voltage
$\rho_{l,cc}$	FC coolant channels coolant density	V_{exp}	Battery exponential voltage
α_T	Coolant isobaric thermal expansion coefficient	V_{full}	Battery fully charge voltage
β	Coolant isothermal bulk modulus	A	Battery exponential zone amplitude
$D_{h,cc}$	FC coolant channels hydraulic diameter	B	Battery exponential zone inverse time constant
$\dot{m}_{avg,cc}$	FC coolant channels average mass flow rate	K	Battery polarization constant
h_{cc}	FC coolant channels heat transfer coefficient	λ_d	Battery charge/discharge efficiency
$\Phi_{work,p}$	Coolant pump power	SOC	Battery state of charge
$\dot{m}_p^{ref}$	Coolant pump reference flow rate	V_a	Motor armature voltage
$k_{P,p}$	Coolant pump proportional control gain	I_a	Motor armature current
$k_{I,p}$	Coolant pump integral control gain	R_{ar}	Motor armature resistance
T_{FC}^{ref}	FC reference temperature	L_a	Motor armature inductance
$\dot{m}_{ct}$	Coolant tank mass flow rate	E_a	Motor back-emf
Φ_{ct}	Coolant tank energy flow rate	T_e	Motor torque
T_L	Motor load torque	$\Delta I_{L,b}$	Boost converter max inductor current ripples
J_m	Rotor inertia	$\Delta V_{out,b}$	Boost converter max output voltage ripples
B_m	Motor viscous friction coefficient	$f_{s,b}$	Boost converter switching frequency
ω_m	Motor rotational speed	$K_{P,b}$	Boost converter proportional control gain
k_t	Motor torque constant	$K_{I,b}$	Boost converter integrative control gain
k_e	Motor back-emf constant	I_{FC}^{ref}	Reference FC current
k_m	Motor constant	$V_{in,bb}$	Buck-Boost converter input voltage
I_a^{ref}	Motor reference armature current	$V_{out,bb}$	Buck-Boost converter output voltage
V_a^{ref}	Motor reference armature voltage	$I_{in,bb}$	Buck-Boost converter input current
ω_m^{ref}	Motor reference rotational speed	$I_{out,bb}$	Buck-Boost converter output current
K_{pc}	Motor current control proportional gain	D_{bb}	Buck-Boost converter duty cycle
K_{ic}	Motor current control integral gain	L_{bb}	Buck-Boost converter input inductance
K_{ps}	Motor speed control proportional gain	C_{bb}	Buck-Boost converter output capacitance
K_{is}	Motor speed control integral gain	$I_{L,bb}$	Buck-Boost converter inductor current
$K_{aw,c}$	Motor current control anti wind-up gain	$K_{aw,s}$	Motor speed control anti wind-up gain
ω_{cc}	Motor current control cross-over frequency	$V_{out,bb}^n$	Buck-Boost converter nominal output voltage
ω_{cs}	Motor speed control cross-over frequency	$I_{out,bb}^n$	Buck-Boost converter nominal output current
$V_{in,b}$	Boost converter input voltage	D_{bb}^n	Buck-Boost converter nominal duty cycle
$V_{out,b}$	Boost converter output voltage	$\Delta I_{L,bb}$	Buck-Boost converter max inductor current ripples
$I_{in,b}$	Boost converter input current	$\Delta V_{out,bb}$	Buck-Boost converter max output voltage ripples
$I_{out,b}$	Boost converter output current	$f_{s,bb}$	Buck-Boost converter switching frequency
D_b	Boost converter duty cycle	$K_{P,bb}$	Buck-Boost converter proportional control gain
L_b	Boost converter input inductance	$K_{I,bb}$	Buck-Boost converter integral control gain
C_b	Boost converter output capacitance	P_{load}	Load power
$V_{out,b}^n$	Boost converter nominal output voltage	$P_{FC,opt}$	FC optimal output power
$I_{out,b}^n$	Boost converter nominal output current	SOC_{high}	High SOC threshold value
D_b^n	Boost converter nominal duty cycle	SOC_{low}	Low SOC threshold value
R_{bus}	DC Bus resistance	$P_{FC,max}$	Maximum FC output power

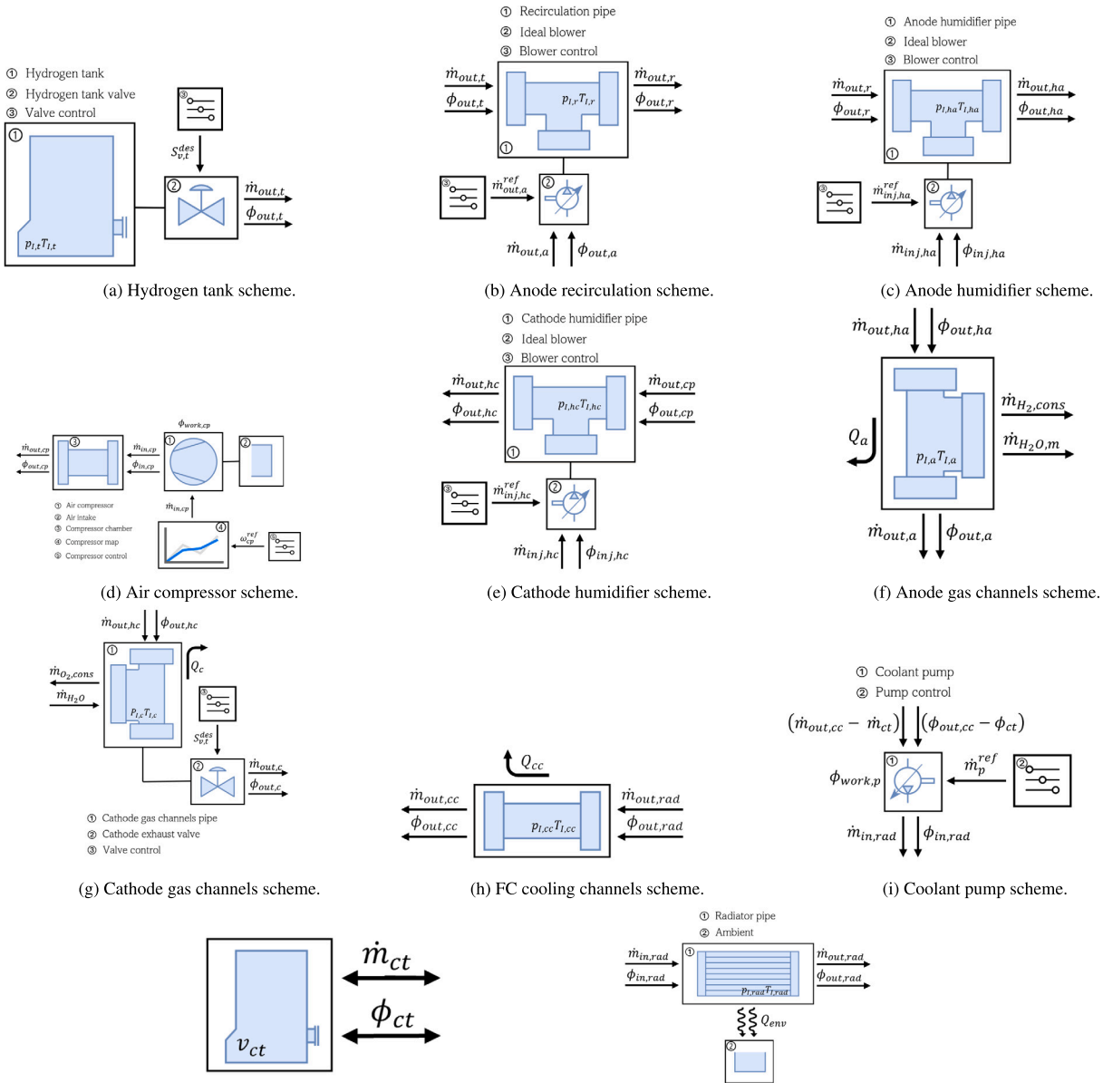

(a) Hydrogen tank scheme.

(b) Anode recirculation scheme.

(c) Anode humidifier scheme.

(d) Air compressor scheme.

(e) Cathode humidifier scheme.

(f) Anode gas channels scheme.

(g) Cathode gas channels scheme.

(h) FC cooling channels scheme.

(i) Coolant pump scheme.

(j) Coolant tank scheme.

(k) Radiator scheme.

Fig. B.1. Exploded view of the Fuel Cell system.

Appendix C. Simscape blocks

See Table C.1.

Table C.1
Simscape blocks used for building the Simscape model.

Component	Implementation	Reference
Fuel cell stack	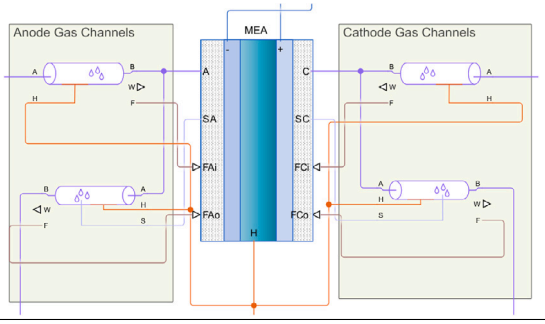	[65]
Anode network	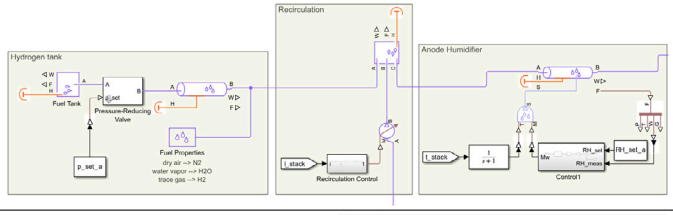	[65]
Cathode network	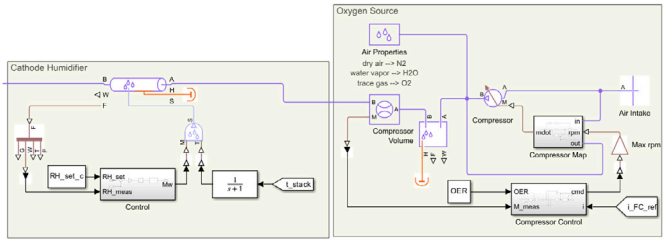	[65]
	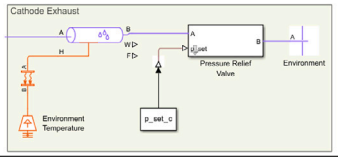	
FC cooling system	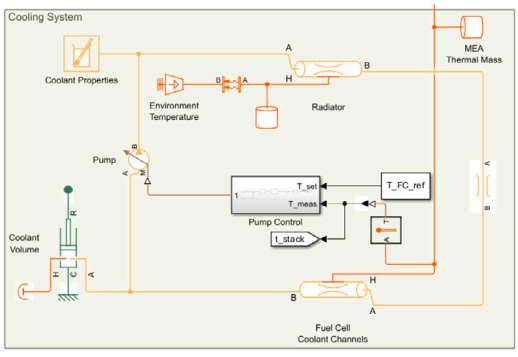	[65]

(continued on next page)

Table C.1 (*continued*).

Battery and power electronics	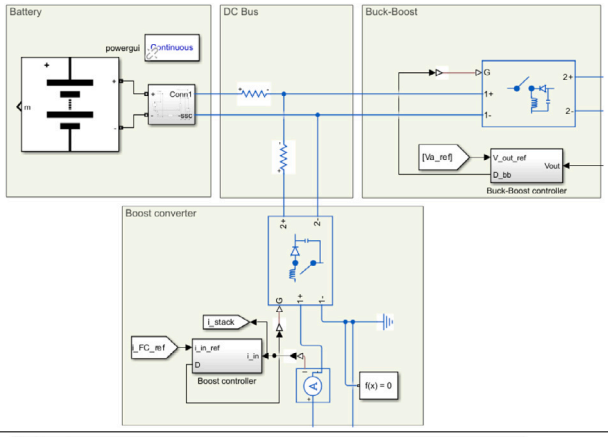	[66–69]
Electric motor	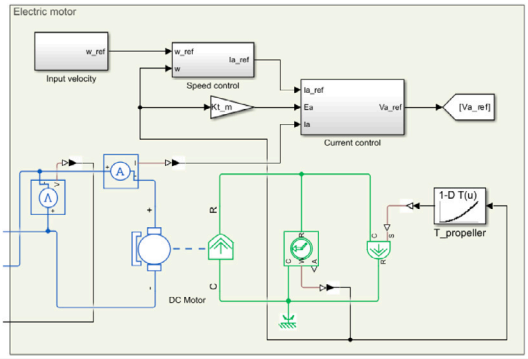	[70,71]

Appendix D. Parameters values used for the simulations

See Table D.1.

Table D.1
Parameters values used for the simulations.

Component	Parameter	Symbol	Value	Unit
Fuel cell	Number of cell in the stack	N_c	400	[–]
	Exchange current density	i_o	$1 \cdot 10^{-4}$	[A/cm^2]
	Max limiting current density	i_L	1,4	[A/cm^2]
	Charge transfer coefficient	α	0.7	[–]
	Fuel cell active area	A_c	280	[cm^2]
	Membrane thickness	t_m	125	[μm]
	Gas diffusion layer thickness	t_{gdl}	250	[μm]
	Dry membrane volume	V_m	0.007	[m^3]
	Dry membrane specific heat	$c_{p,m}$	870	[J/(kg*K)]
	Dry membrane density	$\rho_{m,dry}$	1800	[kg/m^3]
	Unit cell active area	A_c	280	[cm^2]
Hydrogen tank	Tank volume	V_t	0.12	[m^3]
	Initial tank pressure	$p_{t,0}$	70	[MPa]
	Initial tank temperature	$T_{t,0}$	20	[°C]
	Anode network reference pressure	p_{anode}^{ref}	0.161325	[MPa]
	Valve discharge coefficient	$C_{d,t}$	0.64	[–]
	Valve proportional gain	$k_{p,vt}$	$-1.57 \cdot 10^{-8}$	[m^2/Pa]
	Valve modulating coefficient	$k'_{v,t}$	$2.1 \cdot 10^{-7}$	[kg/(Pa*s)]
Anode recirculation	Volume	V_r	$1.25 \cdot 10^{-4}$	[m^3]
	Cross-sectional area	S_r	$7.854 \cdot 10^{-5}$	[m^2]
	Outlet flow gain	$k_{f,r}$	$4 \cdot 10^{-5}$	[kg/(Pa*s)]
	Blower proportional control gain	$k_{p,r}$	0.002	[1/A]
	Blower proportional control gain	$k'_{p,r}$	0.01	[kg/s]
	Blower control constant	c_r	0.2	[–]

(*continued on next page*)

Table D.1 (*continued*).

Component	Parameter	Symbol	Value	Unit
Anode humidifier	Volume	V_{ha}	$4.91 \cdot 10^{-4}$	[m^3]
	Cross-sectional area	S_{ha}	0.002	[m^2]
	Outlet flow gain	$k_{f,ha}$	$6 \cdot 10^{-5}$	[kg/(Pa*s)]
	Proportional control gain	$k_{p,ha}$	0.1	[kg/s]
	Relative humidity setpoint	RH_{set}	1	[–]
Air compressor	Volume	V_{cp}	0.0003	[m^3]
	Inlet cross-sectional area	$S_{cp,in}$	0.002	[m^2]
	Outlet cross-sectional area	$S_{cp,out}$	0.002	[m^2]
	Outlet flow gain	$k_{f,cp}$	$4 \cdot 10^{-3}$	[kg/(Pa*s)]
	Oxygen Excess Ratio (OER)	λ_{O_2}	2.5	[–]
	Proportional control gain	$k_{P,cp}$	5	[s/kg]
	Integral control gain	$k_{I,cp}$	0.5	[1/kg]
	Environmental pressure	p_{env}	0.101325	[MPa]
	Environmental temperature	T_{env}	20	[°C]
	Environmental relative humidity	RH_{env}	0.5	[–]
	Environmental O_2 mass fraction	$x_{O_2,env}$	0.23	[–]
	Pressure ratios vector	p_{ratio}^{LUT}	[1 1.25 1.5 1.75 2]	[–]
	Angular velocity vector	ω_{cp}^{LUT}	[0 1800 3600]	[rpm]
	Corrected flow rate matrix	$\dot{m}_{corr}^{LUT}$	[0 0.05 0.1 ; 0 0.0375 0.075 ; 0 0.025 0.05 ; 0 0.0125 0.025 ; 0 0 0] * 4	[kg/s]
Cathode humidifier	Volume	V_{hc}	$4.91 \cdot 10^{-4}$	[m^3]
	Cross-sectional area	S_{hc}	0.002	[m^2]
	Outlet flow gain	$k_{f,hc}$	$6 \cdot 10^{-5}$	[kg/(Pa*s)]
	Proportional control gain	$k_{p,hc}$	0.1	[kg/s]
Anode gas channels	Volume	V_a	0.0535	[m^3]
	Cross-sectional area	S_a	0.32	[m^2]
	Length	l_a	0.1673	[m]
	Unit cell width	$w_{ch,a}$	0.01	[m]
	Number of unit cell	$N_{ch,a}$	8	[–]
	Surface area	$S_{surf,a}$	21.42	[m^2]
	Hydraulic diameter	$D_{h,a}$	0.01	[m]
Cathode gas channels	Volume	V_c	0.0535	[m^3]
	Cross-sectional area	S_c	0.32	[m^2]
	Length	l_c	0.1673	[m]
	Unit cell width	$w_{ch,c}$	0.01	[m]
	Number of unit cell	$N_{ch,c}$	8	[–]
	Surface area	$S_{surf,c}$	21.42	[m^2]
	Hydraulic diameter	$D_{h,c}$	0.01	[m]
	Valve discharge coefficient	$C_{d,t}$	0.64	[–]
	Valve control proportional gain	$k_{p,c}$	$1.28 \cdot 10^{-8}$	[1/Pa]
	Valve control proportional gain	$k'_{p,c}$	$1.964 \cdot 10^{-3}$	[m^2]
	Valve adding constant	c_c	$1 \cdot 10^{-8}$	[–]
	Cathode network reference pressure	$p_{cathode}^{ref}$	0.161325	[MPa]
FC coolant channels	Volume	V_{cc}	0.004	[m^3]
	Cross-sectional area	S_{cc}	0.002	[m^2]
	Length	l_{cc}	2.01	[m]
	Unit cell width	w_{cc}	0.01	[m]
	Number of unit cell	$N_{p,cc}$	12	[–]
	Number of unit cell	$N_{l,cc}$	20	[–]
	Surface area	$S_{surf,cc}$	1.61	[m^2]
	Hydraulic diameter	$D_{h,cc}$	0.01	[m]
	Outlet flow gain	$k_{f,cc}$	$1 \cdot 10^{-4}$	[kg/(Pa*s)]
Radiator	Volume	V_{cc}	$9.38 \cdot 10^{-4}$	[m^3]
	Cross-sectional area	S_{rad}	$9.38 \cdot 10^{-4}$	[m^2]
	Mass	m_{rad}	3.4	[kg]
	Specific heat	$c_{p,rad}$	910	[J/(kg*K)]
	Convective heat transfer coefficient	k_{rad}	300	[W/K/m^2]
	Surface area	$S_{surf,rad}$	1.33	[m^2]
	Hydraulic diameter	$D_{h,cc}$	0.0028	[m]
Coolant tank	Outlet flow gain	$k_{f,r}$	$1 \cdot 10^{-3}$	[kg/(Pa*s)]
	Initial tank volume	$V_{ct,0}$	0.0081	[m^3]
	Cross-sectional area	S_{ct}	0.1	[m^2]
Coolant pump	FC reference temperature	T_{FC}^{ref}	80	[°C]
	Pump proportional control gain	$k_{P,p}$	0.2	[kg/(s°C)]
	Pump integral control gain	$k_{I,p}$	0.01	[kg/(s^2°C)]

(*continued on next page*)

Table D.1 (*continued*).

Component	Parameter	Symbol	Value	Unit
Battery	Nominal voltage	V_{nom}	409.6	[V]
	Stored energy	E_{bat}	20.48	[kWh]
	Rated capacity	Q_{rated}	50	[Ah]
	Nominal capacity	Q_{nom}	45.2	[Ah]
	Exponential capacity	Q_{exp}	2.47	[Ah]
	Maximum capacity	Q_{max}	51.7	[Ah]
	Exponential voltage	V_{exp}	442.5	[V]
	Fully charge voltage	V_{full}	476.8	[V]
	Constant voltage	V_0	444.3	[V]
	Internal resistance	R_{int}	0.082	[Ω]
	Exponential zone amplitude	A	34.27	[V]
	Exponential zone inverse time constant	B	1.217	[Ah^1]
	Polarization constant	K	0.067	[V/Ah]
	Coulombic efficiency	λ_c	1.039	[–]
Electric motor	Rated output power	$P_{m,rared}$	110	[kW]
	Motor efficiency	η_m	0.92	[–]
	Rated armature voltage	$V_{a,rated}$	520	[V]
	Rated motor velocity	$\omega_{m,rated}$	3220	[rpm]
	Rated armature current	$I_{a,rated}$	224	[A]
	Rated torque	$T_{e,rated}$	326	[N m]
	Armature resistance	R_{ar}	58.5	[mΩ]
	Armature inductance	L_a	1.03	[mH]
	Rotor inertia	J_m	0.07	[kg*m^2]
	Rotor viscous friction	B_m	0.01	[N m/(rad/s)]
	Motor constant	k_m	1.456	[N m/A]
	Current control bandwidth	ω_{cc}	1000	[Hz]
	Current control proportional gain	K_{pc}	1.03	[V/A]
	Current control integral gain	K_{ic}	58.5	[V/(A*s)]
	Speed control bandwidth	ω_{cs}	200	[Hz]
	Speed control proportional gain	K_{ps}	0.35	[kg*m^2]
	Speed control integral gain	K_{is}	14	[kg*m^2/s]
Boost converter	Input inductance	L_b	20	[μH]
	Output capacitance	C_b	500	[μF]
	Switching frequency	$f_{s,b}$	$50 \cdot 10^3$	[Hz]
	Proportional control gain	$K_{P,b}$	0.01	[1/A]
	Integral control gain	$K_{I,b}$	0.1	[1/(A*s)]
Buck-Boost converter	Input inductance	L_{bb}	50	[μH]
	Output capacitance	C_{bb}	2000	[μF]
	Switching frequency	$f_{s,bb}$	$50 \cdot 10^3$	[Hz]
	Proportional control gain	$K_{P,bb}$	0.01	[1/A]
	Integral control gain	$K_{I,bb}$	0.1	[1/(A*s)]
EMS	Optimal FC power	$P_{FC,opt}$	75	[kW]
	Maximum FC power	$P_{FC,max}$	115	[kW]
	Initial battery SOC	SOC_{in}	95	[%]
	High battery SOC	SOC_{high}	80	[%]
	Low battery SOC	SOC_{low}	40	[%]
DC bus	Bus resistance	R_{Bus}	0.01	[Ω]

Data availability

The data were made open source on Github.

References

[1] Kourougianni F, Arsalis A, Olympios AV, Yiasoumas G, Konstantinou C, Papanastasiou P, Georghiou GE. A comprehensive review of green hydrogen energy systems. Renew Energy 2024;231:120911. http://dx.doi.org/10.1016/j.renene.2024.120911.

[2] Agency UEP. Sources of greenhouse gas emissions. 2022, URL https://www.epa.gov/ghgemissions/sources-greenhouse-gas-emissions. [Accessed 05 November 2024].

[3] Olabi AG, Wilberforce T, Abdelkareem MA. Fuel cell application in the automotive industry and future perspective. Energy 2021;214:118955. http://dx.doi.org/10.1016/j.energy.2020.118955.

[4] Aminudin MA, Kamarudin SK, Lim BH, Majilan EH, Masdar MS, Shaari N. An overview: Current progress on hydrogen fuel cell vehicles. Int J Hydrog Energy 2023;48:4371–88. http://dx.doi.org/10.1016/j.ijhydene.2022.10.156.

[5] Pielecha I, Cieślik W, Szałek A. The use of electric drive in urban driving conditions using a hydrogen powered vehicle – Toyota Mirai. Combust Engines 2018;172(1):51–8. http://dx.doi.org/10.19206/CE-2018-106.

[6] Yartys VA, Lototskyy MV, Linkov V, Pasupathi S, Davids MW, Tolj I, Radica G, Denys RV, Eriksen J, Taube K, von Colbe JB, Capurso G, Dornheim M, Smith F, Mathebula D, Swanepoel D, Suwarno S. HYDRIDE4MOBILITY: An EU HORIZON 2020 project on hydrogen powered fuel cell utility vehicles using metal hydrides in hydrogen storage and refuelling systems. Int J Hydrog Energy 2021;35896–909. http://dx.doi.org/10.1016/j.ijhydene.2021.01.190.

[7] Gou B, Na W, Diong B. Fuel cells: Dynamic modeling and control with power electronics applications. 2nd ed.. CRC Press; 2016.

[8] Vu H, Chang D. Optimising computational efficiency in dynamic modelling of proton exchange membrane fuel cell power systems using NARX network. Energy Convers Manag: X 2025;26:100908. http://dx.doi.org/10.1016/J.ECMX.2025.100908.

[9] Wang Y, Yang X, Sun Z, Chen Z. A systematic review of system modeling and control strategy of proton exchange membrane fuel cell. Energy Rev 2024;3(1):100054. http://dx.doi.org/10.1016/j.enrev.2023.100054.

[10] Das SK, Gibson HA. Three dimensional multi-physics modeling and simulation for assessment of mass transport impact on the performance of a high temperature polymer electrolyte membrane fuel cell. J Power Sources 2021;499:229844. http://dx.doi.org/10.1016/J.JPOWSOUR.2021.229844.

[11] Edwards H, Pereira MP, Gharaie S, Omrani R, Shabani B. Computational fluid dynamics modelling of proton exchange membrane fuel cells: Accuracy and time efficiency. Int J Hydrog Energy 2024;50:682–710. http://dx.doi.org/10.1016/J.IJHYDENE.2023.09.004.

[12] Yakubu AU, Qingsheng L, Kai M, Jinwei C, Mohammed OAA, Zhao J, Jiang Q, Ye X, Liu J, Yu Q, Aurangzeb M, Xiong S. Modeling, optimization, and

thermal management strategies of hydrogen fuel cell systems. Results Eng 2025;27:105924. http://dx.doi.org/10.1016/J.RINENG.2025.105924.
[13] Robin C, Gerard M, D'Arbigny J, Schott P, Jabbour L, Bultel Y. Development and experimental validation of a PEM fuel cell 2D-model to study heterogeneities effects along large-area cell surface. Int J Hydrog Energy 2015;40:10211–30. http://dx.doi.org/10.1016/J.IJHYDENE.2015.05.178.
[14] Xie B, Zhang G, Jiang Y, Wang R, Sheng X, Xi F, Zhao Z, Chen W, Zhu Y, Wang Y, Wang H, Jiao K. "3D+1D" modeling approach toward large-scale PEM fuel cell simulation and partitioned optimization study on flow field. ETransportation 2020;6:100090. http://dx.doi.org/10.1016/J.ETRAN.2020.100090.
[15] Gass R, Li Z, Outbib R, Jemei S, Hissel D. An advanced 1D physics-based model for PEM hydrogen fuel cells with enhanced overvoltage prediction. Int J Hydrog Energy 2025;97:1108–25. http://dx.doi.org/10.1016/J.IJHYDENE.2024.11.374.
[16] Jay T. Pukrushpan HP. Control of fuel cell power systems. Springer; 2004.
[17] Hosseinzadeh E, Rokni M, Rabbani A, Mortensen HH. Thermal and water management of low temperature proton exchange membrane fuel cell in fork-lift truck power system. Appl Energy 2013;104:434–44. http://dx.doi.org/10.1016/J.APENERGY.2012.11.048.
[18] Dashti I, Asghari S, Goudarzi M, Meyer Q, Mehrabani-Zeinabad A, Brett DJ. Optimization of the performance, operation conditions and purge rate for a dead-ended anode proton exchange membrane fuel cell using an analytical model. Energy 2019;179:173–85. http://dx.doi.org/10.1016/J.ENERGY.2019.04.118.
[19] Zhang Q, Tong Z, Tong S, Cheng Z. Modeling and dynamic performance research on proton exchange membrane fuel cell system with hydrogen cycle and dead-ended anode. Energy 2021;218:119476. http://dx.doi.org/10.1016/J.ENERGY.2020.119476.
[20] Kim DK, Min HE, Kong IM, Lee MK, Lee CH, Kim MS, Song HH. Parametric study on interaction of blower and back pressure control valve for a 80-kW class PEM fuel cell vehicle. Int J Hydrog Energy 2016;41:17595–615. http://dx.doi.org/10.1016/J.IJHYDENE.2016.07.218.
[21] Hu B, Qu Z, Tao W. A comprehensive system-level model for performance evaluation of proton exchange membrane fuel cell system with dead-ended anode mode. Appl Energy 2023;347:121327. http://dx.doi.org/10.1016/j.apenergy.2023.121327, URL https://linkinghub.elsevier.com/retrieve/pii/S0306261923006918.
[22] Zecchi L, Sandrini G, Gadola M, Chindamo D, Barbucci A. Modeling of a hybrid fuel cell powertrain with power split logic for onboard energy management using a longitudinal dynamics simulation tool. Energies 2022. http://dx.doi.org/10.3390/en15176228, URL https://doi.org/10.3390/en15176228.
[23] Sun G, Sam P, Lin Z. Modeling and simulation of PEM fuel cell / battery hybrid vehicle. Xitong Fangzhen Xuebao J Syst Simul 2018;30:4816–24. http://dx.doi.org/10.16182/J.ISSN1004731X.JOSS.201812041, URL https://www.researchgate.net/publication/332712685_Modeling_and_Simulation_of_PEM_Fuel_Cell_Battery_Hybrid_Vehicle.
[24] De Lorenzo G, Piraino F, Longo F, Tinè G, Boscaino V, Panzavecchia N, Caccia M, Fragiacomo P. Modelling and performance analysis of an autonomous marine vehicle powered by a fuel cell hybrid powertrain. Energies 2022;15(19). http://dx.doi.org/10.3390/en15196926.
[25] Touileb R, Abbou A. Simulation and optimization of hydrogen consumption in a fuel cell/battery hybrid vehicle. Int J Power Electron Drive Syst (IJPEDS) 2023;14:662. http://dx.doi.org/10.11591/ijpeds.v14.i2.pp662-672.
[26] Singh M, Srivastava R, Fuenmayor E, Kuts V, Qiao Y, Murray N, Devine D. Applications of digital twin across industries: A review. Appl Sci 2022;12:5727. http://dx.doi.org/10.3390/app12115727.
[27] Oladosu TL, Pasupuleti J, Kiong TS, Koh SPJ, Yusaf T. Energy management strategies, control systems, and artificial intelligence-based algorithms development for hydrogen fuel cell-powered vehicles: A review. 2024, http://dx.doi.org/10.1016/j.ijhydene.2024.02.284.
[28] Miretti F, Misul D, Gennaro G, Ferrari A. Hybridizing waterborne transport: Modeling and simulation of low-emissions hybrid waterbuses for the city of Venice. Energy 2022;244(Part B):123183. http://dx.doi.org/10.1016/j.energy.2022.123183.
[29] Sürer MG, Arat HT. Advancements and current technologies on hydrogen fuel cell applications for marine vehicles. Int J Hydrog Energy 2022;47(45):19865–75. http://dx.doi.org/10.1016/J.IJHYDENE.2021.12.251.
[30] Fu Z, Lu L, Zhang C, Xu Q, Zhang X, Gao Z, Li J. Fuel cell and hydrogen in maritime application: A review on aspects of technology, cost and regulations. Sustain Energy Technol Assess 2023;57(October 2022):103181. http://dx.doi.org/10.1016/j.seta.2023.103181.
[31] Brusasco A. A computational efficient, multi-domain numerical framework for modelling fuel cell — battery powered powertrains. 2025, URL https://github.com/AlessandroBrusasco/A-computational-efficient-numerical-framework-for-modeling-fuel-cell-battery-powered-powertrain. Commit a38a9f9.
[32] Li W, Wei X, Wang J, Wang X. Construction of nitrogen content observer for fuel cell hydrogen circuit based on anode recirculation mode. World Electr Veh J 2023;14. http://dx.doi.org/10.3390/wevj14050131.
[33] White FM. Fluid mechanics. McGraw-Hill; 2011, http://dx.doi.org/10.13140/RG.2.2.21339.62244.
[34] Young DF, Munson BR, Okiishi T. A brief introduction to fluid mechanics. 5th ed.. John Wiley & Sons; 2011.
[35] Cengel Y. GA. Heat and mass transfer. McGraw-Hill; 2007.
[36] Martin D, Karel P, Stanislav S. Gnielinski's correlation and a modern temperature-oscillation method for measuring heat transfer coefficients. EPJ Web Conf 2022;269:1009. http://dx.doi.org/10.1051/epjconf/202226901009.
[37] Greitzer EM, Bonnefoy PA, delaRosaBlanco E, Dorbian CS, Drela M, Hall DK, Hansman RJ, Hileman JI, Liebeck RH, Lovegren JA, Mody P, Pertuzé JA, Sato S, Spakovszky ZS, Tan CS, Hollman JS, Duda J, Fitzgerald N, Houghton JW, Kerrebrock JL, Kiwada G, Kordonowy D, Parrish JC, Tylko J, Wen EA. N+3 aircraft concept designs and trade studies. Volume 2. In: Appendices-design methodologies for aerodynamics, structures, weight, and thermodynamic cycles. 2010, p. 1–81, URL https://api.semanticscholar.org/CorpusID:107448260.
[38] Molaeimanesh GR, Gholam Reza FM, authorTorabi. Fuel cell modeling and simulation : from microscale to macroscale. 1st ed.. Amsterdam: Elsevier; 2023.
[39] Li M, Lu J, Hu Y, Gao J. Oxygen excess ratio controller design of PEM fuel cell. IFAC Pap 2018;51:493–8. http://dx.doi.org/10.1016/j.ifacol.2018.10.108.
[40] Spiegel C. PEM fuel cell modeling and simulation using matlab. Academic Press; 2008, http://dx.doi.org/10.1016/B978-0-12-374259-9.X5001-0.
[41] Li Z, Zheng Z, Xu L, Lu X. A review of the applications of fuel cells in microgrids: opportunities and challenges. BMC Energy 2019;1. http://dx.doi.org/10.1186/s42500-019-0008-3.
[42] Husar A, Strahl S, Riera J. Experimental characterization methodology for the identification of voltage losses of PEMFC: Applied to an open cathode stack. Int J Hydrog Energy 2012;37:7309–15. http://dx.doi.org/10.1016/j.ijhydene.2011.11.130.
[43] JE L, Dicks A. Fuel cell system explained. John Wiley & Sons Ltd; 2013, http://dx.doi.org/10.1002/9781118878330.
[44] AA A, Azmy A. Dynamic modelling of proton exchange membrane fuel cells for electric vehicle applications. J Petroleum Environ Biotechnol 2014;5. http://dx.doi.org/10.4172/2157-7463.1000169.
[45] Springer TE, Zawodzinski TA, Gottesfeld S. Polymer electrolyte fuel cell model. J Electrochem Soc 1991;138:2334. http://dx.doi.org/10.1149/1.2085971.
[46] Dutta S, Shimpalee S, Zee JV. Numerical prediction of mass-exchange between cathode and anode channels in a PEM fuel cell. Int J Heat Mass Transf Int J Heat Mass Transfer 2001;44:2029–42. http://dx.doi.org/10.1016/S0017-9310(00)00257-X.
[47] Fu Y, Jiang Y, Dutta A, Mohanram A, Pietras JD, Bazant MZ. Multicomponent gas diffusion in porous electrodes. 2014, arXiv:1409.2965. URL https://arxiv.org/abs/1409.2965.
[48] Iranzo A, Boillat P. Liquid water distribution patterns featuring back-diffusion transport in a PEM fuel cell with neutron imaging. Int J Hydrog Energy 2014;39:17240–5. http://dx.doi.org/10.1016/j.ijhydene.2014.08.042.
[49] Kumar RR, Bharatiraja C, Udhayakumar K, Devakirubakaran S, Sekar KS, Mihet-Popa L. Advances in batteries, battery modeling, battery management system, battery thermal management, SOC, SOH, and charge/discharge characteristics in EV applications. IEEE Access 2023;11:105761–809. http://dx.doi.org/10.1109/ACCESS.2023.3318121.
[50] Zheng S, Teh J, Alharbi B, Lai C-M. A review of equivalent-circuit model, degradation characteristics and economics of Li-ion battery energy storage system for grid applications. J Energy Storage 2024;101:113908. http://dx.doi.org/10.1016/j.est.2024.113908.
[51] Fan C, Liu K, Ren Y, Peng Q. Characterization and identification towards dynamic-based electrical modeling of lithium-ion batteries. J Energy Chem 2024;92:738–58. http://dx.doi.org/10.1016/j.jechem.2024.01.040.
[52] Saw LH, Somasundaram K, Ye Y, Tay AAO. Electro-thermal analysis of lithium iron phosphate battery for electric vehicles. J Power Sources 2014;249:231–8. http://dx.doi.org/10.1016/j.jpowsour.2013.10.052.
[53] Tremblay O, Dessaint L-A. Experimental validation of a battery dynamic model for EV applications. World Electr Veh J 2009;3:289–98. http://dx.doi.org/10.3390/wevj3020289.
[54] Tremblay O, Dessaint LA, Dekkiche AI. A generic battery model for the dynamic simulation of hybrid electric vehicles. In: 2007 IEEE vehicle power and propulsion conference. 2007, p. 284–9. http://dx.doi.org/10.1109/VPPC.2007.4544139.
[55] Hussein HM, Aghmadi A, Abdelrahman MS, Rafin SMSH, Mohammed O. A review of battery state of charge estimation and management systems: Models and future prospective. WIREs Energy Environ 2024;13. http://dx.doi.org/10.1002/wene.507.
[56] Derammelaere S, Haemers M, Viaene JD, Verbelen F, Stockman K. A quantitative comparison between BLDC, PMSM, brushed DC and stepping motor technologies. In: 2016 19th international conference on electrical machines and systems. ICEMS, 2016, p. 1–5.
[57] Yildiz AB. Electrical equivalent circuit based modeling and analysis of direct current motors. Int J Electr Power Energy Syst 2012;43:1043–7. http://dx.doi.org/10.1016/j.ijepes.2012.06.063.
[58] Kim S-H. Electric motor control: DC, AC, and BLDC motors. Elsevier; 2017, p. 1–426.
[59] Franklin GF, Powell JD. Feedback control of dynamic systems, vol. 5, Upper Saddle River, N.J.: Pearson Prentice Hall; 2006.
[60] Peng Y, Vrančić D, Hanus R. Antiwindup, bumpless, and conditioned transfer techniques for PID controllers. Control Syst IEEE 1996;16:48–57. http://dx.doi.org/10.1109/37.526915.
[61] Wu KC. Pulse width modulated DC-DC converters. Boston, MA: Springer US; 1997, http://dx.doi.org/10.1007/978-1-4615-6021-0.

[62] Han J, Charpentier J-F, Tang T. An energy management system of a fuel cell/battery hybrid boat. Energies 2014;7:2799–820. http://dx.doi.org/10.3390/en7052799.

[63] An T, Truong A, Pham M, Do TC, Lee H-H, Ahn KK. Comprehensive control strategy and verification for PEM fuel cell/battery/supercapacitor hybrid power source. Int J Precis Eng Manuf Green Technol 2022;10. http://dx.doi.org/10.1007/s40684-022-00498-w.

[64] Diana M, Martoccia L, Fontanesi S, Mangeruga V, d'Adamo A. A MATLAB script and a methodology for the powertrain design of a fuel cells-battery hybrid electric supercar. Energy Convers Manag: X 2024;23:100663. http://dx.doi.org/10.1016/j.ecmx.2024.100663.

[65] MathWorks I. PEM fuel cell system. 2022, URL https://www.mathworks.com/help/simscape/ug/pem-fuel-cell-system.html. [Accessed 05 March 2025].

[66] MathWorks. Boost converter. 2024, URL https://it.mathworks.com/help/sps/ref/boostconverter.html. [Accessed 05 March 2025].

[67] MathWorks. Buck-boost converter. 2024, URL https://it.mathworks.com/help/sps/ref/buckboostconverter.html. [Accessed 05 March 2025].

[68] MathWorks. Resistor. 2024, URL https://it.mathworks.com/help/simscape/ref/resistor.html. [Accessed 05 March 2025].

[69] MathWorks. Battery. 2024, URL https://it.mathworks.com/help/sps/powersys/ref/battery.html. [Accessed 05 March 2025].

[70] MathWorks. DC motor. 2024, URL https://it.mathworks.com/help/sps/ref/dcmotor.html. [Accessed 05 March 2025].

[71] MathWorks. Ideal torque source. 2024, URL https://it.mathworks.com/help/simscape/ref/idealtorquesource.html. [Accessed 05 March 2025].